STATE OF THE CLIMATE IN 2024

ANTARCTICA AND THE SOUTHERN OCEAN

M. N. Raphael and K. R. Clem, Eds.

Special Online Supplement to the *Bulletin of the American Meteorological Society* Vol. 106, No. 8, August, 2025

https://doi.org/10.1175/BAMS-D-25-0087.1

Corresponding author: Marilyn N. Raphael / raphael@geog.ucla.edu

STATE OF THE CLIMATE IN 2024
Antarctica and the Southern Ocean

Editors

Jessica Blunden
James Reagan

Chapter Editors

Anthony Arguez
Josh Blannin
Peter Bissolli
Kyle R. Clem
Howard J. Diamond
Matthew L. Druckenmiller
Robert J. H. Dunn
Catherine Ganter
Nadine Gobron
Gregory C. Johnson
Rick Lumpkin
Rodney Martinez
Ademe Mekonnen
Twila A. Moon
Gary A. Morris
Marilyn N. Raphael
Carl J. Schreck III
Laura Stevens
Richard L. Thoman
Kate M. Willett
Zhiwei Zhu

Technical Editor

Lukas Noguchi

BAMS Special Editor for Climate

Timothy DelSole

American Meteorological Society

Cover Credit:
Dr. Naomi Ochwat of the University of Colorado (right, blue jacket) and Ms. Liliana Margonari of the University of Buenos Aires (left, orange jacket) on a rock ledge overlooking Crane Glacier in the Antarctic Peninsula on 26 February 2024. The field work was supported by NASA grant 80NSSC22K0386. The team was supported by Argentina's Direction National Antarctica. Photo credit: Dr. Ted Scambos, University of Colorado Boulder

How to cite this document:
Antarctica and the Southern Ocean is one chapter from the *State of the Climate in 2024* annual report and is available from https://doi.org/10.1175/BAMS-D-25-0087.1. Compiled by NOAA's National Centers for Environmental Information, *State of the Climate in 2024* is based on contributions from scientists from around the world. It provides a detailed update on global climate indicators, notable weather events, and other data collected by environmental monitoring stations and instruments located on land, water, ice, and in space. The full report is available from https://doi.org/10.1175/2025BAMSStateoftheClimate.1.

Citing the complete report:
Blunden, J. and J. Reagan, Eds., 2025: "State of the Climate in 2024". Bull. Amer. Meteor. Soc., 106 (8), Si–S513 https://doi.org/10.1175/2025BAMSStateoftheClimate.1.

Citing this chapter:
Raphael, M. N. and K. R. Clem, Eds., 2025: Antarctica and the Southern Ocean [in "State of the Climate in 2024"]. Bull. Amer. Meteor. Soc., 106 (8), S357–S400, https://doi.org/10.1175/BAMS-D-25-0087.1.

Citing a section (example):
MacFerrin, M., T. Mote, A. F. Banwell, and T. Scambos, 2025: Ice sheet seasonal melt extent and duration [in "State of the Climate in 2024"]. Bull. Amer. Meteor. Soc., 106 (8), S372–S374, https://doi.org/10.1175/BAMS-D-25-0087.1.

Editor and Author Affiliations (alphabetical by name)

Adjou, Mohamed, ISEN Engineering School, LaBISEN, Knowledge Learning and Information Modeling (KLaIM), Brest, France; University of Brest, Institut Universitaire Européen de la Mer (IUEM) UAR3113, Plouzané, France

Adusumilli, Susheel, Scripps Institution of Oceanography, University of California, San Diego, La Jolla, California

Amory, Charles, Université Grenoble Alpes, Institut des Géosciences de l'Environnement, IRD, CNRS, Grenoble INP, Grenoble, France

Bahrami, Mahsa, Department of Geography, Pennsylvania State University, State College, Pennsylvania

Baiman, Rebecca, Department of Atmospheric and Oceanic Sciences, University of Colorado Boulder, Boulder, Colorado

Banwell, Alison F., Earth Science and Observation Center, Cooperative Institute for Research in Environmental Sciences (ESOC/CIRES), University of Colorado Boulder, Boulder, Colorado

Barreira, Sandra, Argentine Naval Hydrographic Service, Buenos Aires, Argentina

Beadling, Rebecca L., Department of Earth and Environmental Science, Temple University, Philadelphia, Pennsylvania

Clem, Kyle R., School of Geography, Environment and Earth Sciences, Victoria University of Wellington, Wellington, New Zealand

Colwell, Steve, British Antarctic Survey, Cambridge, United Kingdom

Coy, Lawrence, Science Systems and Applications, Inc., Lanham, Maryland; NASA Goddard Space Flight Center, Greenbelt, Maryland

Datta, Rajashree T., Department of Civil Engineering and Geosciences, TU Delft, The Netherlands

De Laat, Jos, Royal Netherlands Meteorological Institute (KNMI), DeBilt, The Netherlands

du Plessis, Marcel, Department of Marine Sciences, University of Gothenburg, Sweden

Fogt, Ryan L., Department of Geography, Ohio University, Athens, Ohio

Fricker, Helen A., Scripps Institution of Oceanography, University of California, San Diego, La Jolla, California

Hancock, Alyce M., Southern Ocean Observing System (SOOS), Institute for Marine and Antarctic Studies (IMAS), University of Tasmania, Hobart, Australia

Johnson, Bryan, NOAA/OAR Earth System Research Laboratory, Global Monitoring Division, Boulder, Colorado; University of Colorado Boulder, Boulder, Colorado

Josey, Simon A., National Oceanography Centre, Southampton, United Kingdom

Keller, Linda M., Antarctic Meteorological Research and Data Center, Space Science and Engineering Center, University of Wisconsin-Madison, Madison, Wisconsin

Kittel, Christoph, Department of Geography, University of Liège, Liège, Belgium; Physical Geography Research Group, Department of Geography, Vrije Universiteit Brussel, Brussels, Belgium

Kramarova, Natalya A., NASA Goddard Space Flight Center, Greenbelt, Maryland

Lait, Leslie R., NASA Ames Research Center, Moffett Field, California

Lazzara, Matthew A., Department of Physical Sciences, School of Arts and Sciences, Madison Area Technical College; Antarctic Meteorological Research and Data Center, Space Science and Engineering Center, University of Wisconsin-Madison, Madison, Wisconsin

Lieser, Jan L., Bureau of Meteorology, Hobart, Australia; Institute for Marine and Antarctic Studies (IMAS), University of Tasmania, Hobart, Australia

MacFerrin, Michael, Earth Science and Observation Center, Cooperative Institute for Research in Environmental Sciences (ESOC/CIRES), University of Colorado Boulder, Boulder, Colorado

MacLennan, Michelle L., British Antarctic Survey, Cambridge, United Kingdom

Massom, Robert A., Australian Antarctic Division, Australian Antarctic Program Partnership (AAPP) and Australian Centre for Excellence in Antarctic Science (ACEAS), Hobart, Australia

Mikolajczyk, David E., Antarctic Meteorological Research and Data Center, Space Science and Engineering Center, University of Wisconsin-Madison, Madison, Wisconsin

Milward, James, Department of Earth and Environmental Science, Temple University, Philadelphia, Pennsylvania

Mote, Thomas L., Department of Geography, University of Georgia, Athens, Georgia

Newman, Paul A., NASA Goddard Space Flight Center, Greenbelt, Maryland

Norton, Taylor, Antarctic Meteorological Research and Data Center, Space Science and Engineering Center, University of Wisconsin-Madison, Madison, Wisconsin

Petropavlovskikh, Irina, NOAA/OAR Earth System Research Laboratory, Global Monitoring Division, Boulder, Colorado; University of Colorado Boulder, Boulder, Colorado

Pezzi, Luciano P., Laboratory of Ocean and Atmosphere Studies (LOA), Earth Observation and Geoinformatics Division (DIOTG), National Institute for Space Research (INPE), São José dos Campos, Brazil

Raphael, Marilyn N., Department of Geography, University of California, Los Angeles, Los Angeles, California

Reid, Phillip, Bureau of Meteorology, Hobart, Australia; Australian Antarctic Program Partnership (AAPP), Hobart, Tasmania, Australia

Ryan-Keogh, Thomas J., Southern Ocean Carbon-Climate Observatory, Council for Scientific and Industrial Research (CSIR), Cape Town, South Africa

Santee, Michelle L., NASA Jet Propulsion Laboratory, Pasadena, California

Scambos, Theodore, Earth Science and Observation Center, Cooperative Institute for Research in Environmental Sciences (ESOC/CIRES), University of Colorado Boulder, Boulder, Colorado

Schulz, Cristina, Department of Marine and Environmental Sciences, Northeastern University, Boston, Massachussetts

Shi, Jia-Rui, Courant Institute of Mathematical Sciences, New York University, New York City, New York

Souza, Everaldo, Federal University of Pará (UFPA), Belém, Brazil

Stammerjohn, Sharon, Institute of Arctic and Alpine Research, University of Colorado Boulder, Boulder, Colorado

Thomalla, Sandy, Southern Ocean Carbon-Climate Observatory, Council for Scientific and Industrial Research (CSIR), Cape Town, South Africa; Marine and Antarctic Research Centre for Innovation and Sustainability, Department of Oceanography, University of Cape Town, Cape Town, South Africa

Trusel, Luke, Department of Geography, Pennsylvania State University, State College, Pennsylvania

Wille, Jonathan D., Institute for Atmospheric and Climate Science, ETH Zürich, Zürich, Switzerland; Institut des Géosciences de l'Environnement, IRD, CNRS, Grenoble INP, Saint Martin d'Hères, France

Editorial and Production Team

Allen, Jessicca, Graphics Support, Cooperative Institute for Satellite Earth System Studies, North Carolina State University, Asheville, North Carolina

Camper, Amy V., Graphics Support, Innovative Consulting and Management Services, LLC, NOAA/NESDIS National Centers for Environmental Information, Asheville, North Carolina

Carroll, Lauren, Content Team Lead, Communications and Outreach, NOAA/NESDIS National Centers for Environmental Information, Asheville, North Carolina

Haley, Bridgette O., Graphics Support, NOAA/NESDIS National Centers for Environmental Information, Asheville, North Carolina

Love-Brotak, S. Elizabeth, Lead Graphics Production, NOAA/NESDIS National Centers for Environmental Information, Asheville, North Carolina

Ohlmann, Laura, Technical Editor, Innovative Consulting and Management Services, LLC, NOAA/NESDIS National Centers for Environmental Information, Asheville, North Carolina

Noguchi, Lukas, Technical Editor, Innovative Consulting and Management Services, LLC, NOAA/NESDIS National Centers for Environmental Information, Asheville, North Carolina

Riddle, Deborah B., Graphics Support, NOAA/NESDIS National Centers for Environmental Information, Asheville, North Carolina

Veasey, Sara W., Visual Communications Team Lead, Communications and Outreach, NOAA/NESDIS National Centers for Environmental Information, Asheville, North Carolina

6. Table of Contents

6. ANTARCTICA AND THE SOUTHERN OCEAN

M. N. Raphael and K. R. Clem, Eds.

a. Overview

—M. N. Raphael and K. R. Clem

In 2024, atmospheric conditions over Antarctica exhibited significant anomalies, and were marked by major surface and stratospheric warming and pressure fluctuations. The first half of the year (January–June) featured persistent below-normal surface pressure over the continent, a distinct zonal wavenumber-3 pattern with three deep atmospheric troughs extending over the Weddell Sea, Prydz Bay, and Ross Ice Shelf, and a positive phase of the Southern Annular Mode, with strong circumpolar westerlies. Surface pressure anomalies in February and April were particularly pronounced, with multiple stations recording record-low pressures.

Strong stratospheric warming occurred in July followed by extreme surface warming in August. The surface warming was likely intensified by a compound event: 1) a strong ridge of surface high pressure along coastal East Antarctica advected warm maritime air into the continental interior, and 2) a significant positive geopotential height and temperature anomaly in the stratosphere propagated downward to the surface. As a result, multiple monthly records for high temperatures and pressure were set in August.

The Antarctic Ice Sheet's surface mass balance (SMB) in 2024 was shaped by contrasting periods of high snowfall and regional drought. The most significant anomaly occurred in May, when extreme snowfall led to record-high SMB gains across much of East and West Antarctica. Enhanced meridional moisture transport and atmospheric river events—which funneled moisture from the South Pacific and Atlantic Oceans toward the continent—supported/generated this extreme snowfall. In contrast, September emerged as the driest September on record, with a severe shortage of snowfall over the ice sheet. This was linked to an anomalously deep and eastward-shifted Amundsen Sea Low, which suppressed precipitation and led to below-average SMB across West Antarctica.

There was continued ice sheet mass loss in the Amundsen Sea sector of West Antarctica, where observations show that thinning has persisted since 1992. Additional losses were observed in the Antarctic Peninsula, particularly near the Larsen C Ice Shelf and Bellingshausen Sea. However, some regions of East Antarctica, notably Dronning Maud Land and Totten Glacier, exhibited localized mass gains due to increased snowfall.

A net Antarctic mass loss of 125 Gt occurred between January and November 2024, exceeding the long-term annual average of 100 Gt per year. Although this loss was not as extreme as in some previous years, it underscored the continued trend of mass decline, particularly in West Antarctica and the Antarctic Peninsula.

Antarctic sea ice remained anomalously low in 2024, with record- or near-record-low extents observed for much of the year. The annual daily minimum sea ice extent was recorded on 18 February at 1.97 million km^2, the third lowest on record. The seasonal cycle was again disrupted, with delayed autumn–winter expansion and an early spring–summer retreat. By late 2024, sea ice conditions began to recover slightly, with overall sea ice extent approaching near-average values in November and December. However, this temporary return to average conditions did not offset the negative trend observed since 2016.

Regionally, the eastern Weddell Sea experienced particularly severe low sea ice coverage, likely due to warmer sea surface temperatures and weakened stratification in the upper ocean. This reduction in sea ice caused increased exposure of coastal regions to oceanic and atmospheric variability. In contrast, the western Weddell Sea and some parts of the Ross and Amundsen Seas

saw temporary sea ice expansion driven by localized cold air outbreaks and persistent southerly winds.

Across the Southern Ocean, sea surface temperatures increased markedly, with positive anomalies persisting through 2024. This continued the positive trend observed since 2005. The western Pacific region showed the greatest increases, especially from February to July. In concert with the sea surface temperatures, ocean heat content also increased to levels higher than previously experienced. The region of greatest increase in sea surface temperatures coincided with the regions of below-average sea ice extent. Chlorophyll, an important marker of ocean biogeochemistry, was at elevated levels during December and January (2023/24), most notably in the Atlantic.

The 2024 Antarctic ozone hole appeared approximately a week later than average on 25 August and was among the least severe ozone holes recorded over the past three decades. It ranked 26th in size, with an average area of 19.6 million km^2 from 7 September to 13 October. The daily minimum ozone concentration was slightly higher than the 1992–2023 mean, and the ozone hole reached its maximum extent later than usual, peaking at 22.4 million km^2 on 28 September. The delayed start to the ozone hole development was due to strong planetary wave activity during mid-May to mid-August, which led to a significant warming of the Antarctic stratosphere in late July to early August and transported ozone into the Antarctic stratosphere, increasing concentrations at a time when they would normally be decreasing. Additionally, average stratospheric temperatures in September and decreased levels of chlorine and bromine in the Antarctic polar vortex led to a 2024 ozone hole that was not as deep nor as extensive as those observed in the early 2000s. The 2024 ozone hole broke up on 21 December, two weeks later than average.

More details on Antarctica's climate, weather, ice, ocean, and ozone are presented below for 2024. Unless otherwise stated, the 2024 anomalies and standard deviations are all based on the 1991–2020 climatology. Note that some sections use different climatology periods due to data availability, while others use non-traditional seasons centered around specific phenomena of interest, such as surface melt (October to April) and the Southern Ocean chlorophyll season (June to July); these details are stated at the beginning of each section. Common geographic regions and place names referenced throughout the chapter are shown in Fig. 6.1.

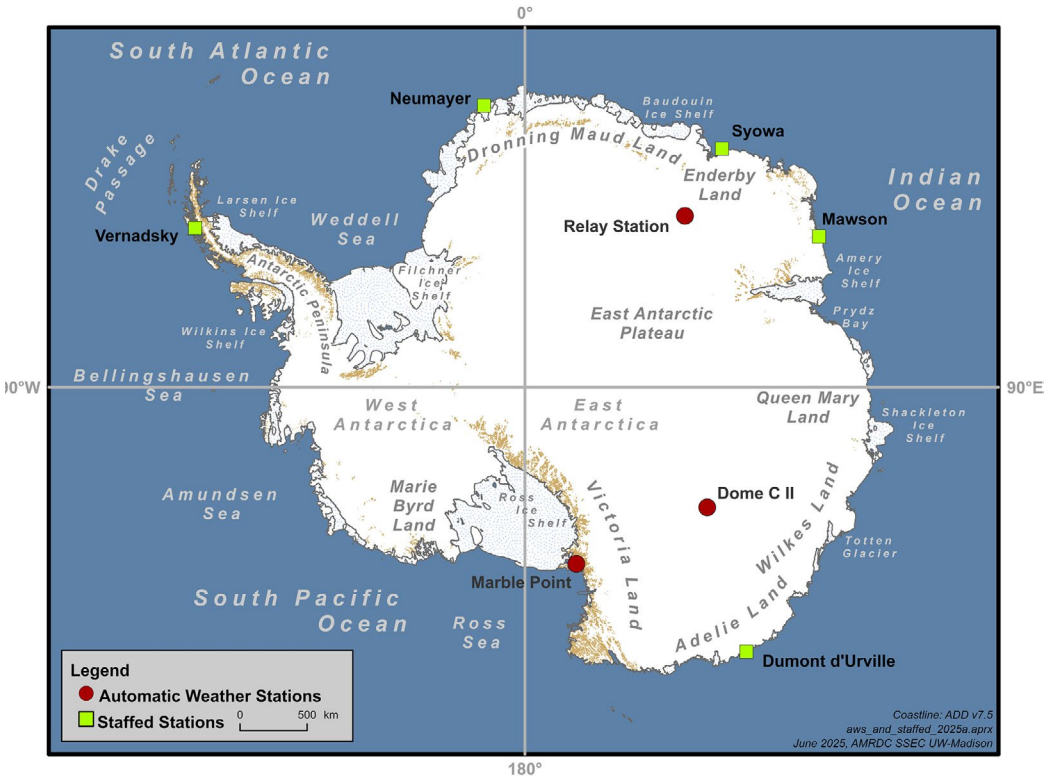

Fig. 6.1. Map of the Antarctic, showing stations, geographic regions, and prominent features discussed in this chapter. Figure courtesy of Samuel Batzli, University of Wisconsin-Madison.

b. Atmospheric circulation and surface observations

—K. R. Clem, T. Norton, D. Mikolajczyk, L. M. Keller, M. A. Lazzara, S. Colwell, S. Barreira, and R. L. Fogt

The Antarctic atmosphere in 2024 was largely characterized by month-to-month variability. The main atmospheric event of the year was a major surface and stratospheric warming during July and August. The surface warming began over the eastern Weddell Sea and Dronning Maud Land in July, triggered by the development of a strong high-pressure system in the southeast Atlantic. August saw the greatest number of new pressure and temperature records during the event as high pressure in the South Atlantic built poleward into East Antarctica, and widespread positive pressure anomalies developed over the remainder of the continent with a likely connection to downward-propagating positive geopotential height anomalies from the stratosphere. For the rest of the year, pressure and temperature were variable from month to month. One notable event occurred in September when a deep cyclone developed over the Antarctic Peninsula, resulting in record-low monthly mean pressure at all long-term staffed weather stations in the region (dating back to 1950). This pattern continued to direct warm northerly airflow over the eastern Weddell Sea and Dronning Maud Land into spring—a persistent feature seen there since March 2023—contributing to more declines and record-low sea ice extents over the eastern Weddell Sea (section 6f), and continued increases in surface mass balance (SMB) over Dronning Maud Land (section 6c).

To investigate these features from 2024 in detail, we employ ERA5 (Hersbach et al. 2020), staffed weather station data from the READER archive (Turner et al. 2004) and automatic weather station (AWS) data from the Antarctic Meteorological Research and Data Center (AMRDC) data repository (AMRDC 2022). First, surface temperature and pressure anomalies from ERA5 were grouped and averaged over four periods of relatively persistent features: January–June, July–August, September–October, and November–December (Fig. 6.2). Figure 6.3 shows the vertical structure of the monthly geopotential height (Fig. 6.3a) and temperature (Fig. 6.3b) anomalies averaged over the polar cap (60°S–90°S) and the monthly circumpolar zonal wind anomalies (Fig. 6.3c) averaged over 50°S–70°S. Observed monthly temperature and pressure anomalies for select staffed and automated weather stations are shown in Fig. 6.4; see Fig. 6.1 for station locations and geographical references made in this section and throughout the

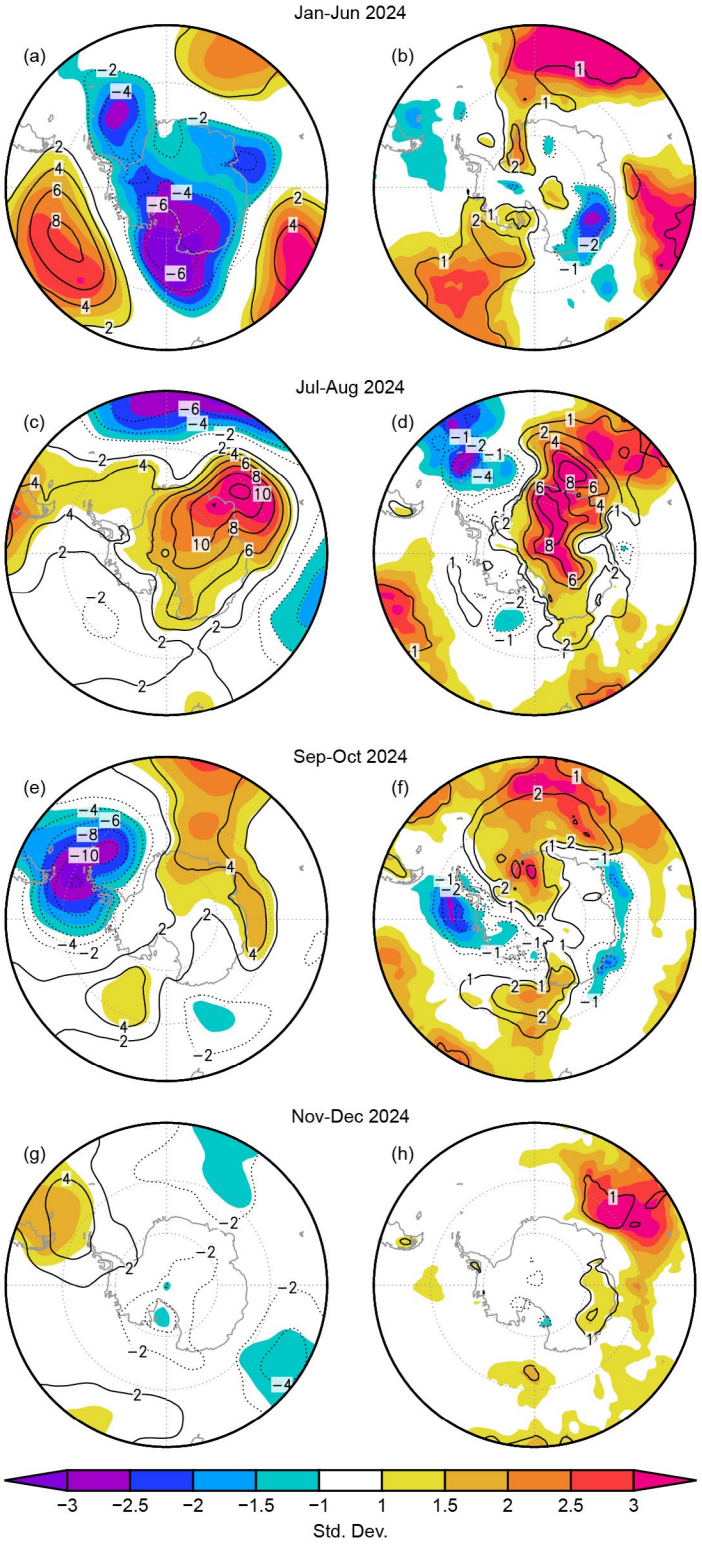

Fig. 6.2. (left) Surface pressure (hPa) and (right) 2-m temperature anomalies (°C) relative to 1991–2020 for (a),(b) Jan–Jun 2024; (c),(d) Jul–Aug 2024; (e),(f) Sep–Oct 2024, and (g),(h) Nov–Dec 2024. Contour interval is 2 for both fields with an additional ±1°C contour added for 2-m temperature; zero contours are omitted. Shading shows the std. dev. of the anomalies. (Source: ERA5)

chapter. All anomalies and standard deviations presented are based on the 1991–2020 climatology.

The first half of the year (January–June) was characterized by below-normal surface pressure over the continent (Fig. 6.2a) accompanied by three deep troughs extending offshore over the Weddell Sea, Prydz Bay, and Ross Ice Shelf/Ross Sea. The three troughs were each flanked by strong high-pressure anomalies (each 2–3 std. dev. above average) along 50°S–60°S—one in the central South Pacific, one south of Africa, and one south of Australia—producing a distinct zonal wavenumber-3 pattern and a positive phase of the Southern Annular Mode (SAM); the SAM index was positive in all six months (Fig. 6.3). Within this period were two months of more pronounced negative pressure anomalies over the polar cap (region south of 60°S) in February and April (as illustrated by the geopotential height anomalies in Fig. 6.3a), with April also seeing a significant strengthening of the circumpolar westerlies to more than 2 std. dev. above average (Fig. 6.3c). Record-low monthly mean pressures were recorded at various stations, including Neumayer in February (since 1981; not shown), and in April at Dumont d'Urville (Fig. 6.4d), Marble Point AWS (Fig. 6.4e), Ferrell AWS (since 1985; not shown), and Gill AWS (since 1981; not shown). In June, McMurdo recorded its lowest monthly pressure on record (since 1956; not shown).

Surface temperature anomalies during January–June reflect the wave-3 structure, with three main regions of above-average temperatures on the eastern sides of the troughs, and below-average temperatures on the western sides. Western Dronning Maud Land and western Marie Byrd Land experienced the most pronounced warming, while below-average temperatures were noted over Adélie Land. Two new temperature records were set: Neumayer recorded its warmest February on record (since 1981), and Dome C II AWS recorded its coldest April on record (since 1980; neither shown). The regionally varying temperature anomalies largely cancel out when averaged over the polar cap (Fig. 6.3b), except in February and March, which stood out with above-average temperatures over the continent.

July and August were marked by two major events: a strong stratospheric warming event in July (section 6h) and a major surface warming event in August (Fig. 6.3b), both of which produced monthly anomalies well over 3 std. dev. above the months' respective climatologies. The dominant surface circulation feature was a strong ridge of high pressure centered along the East Antarctic coast between 40°E and 60°E (Fig. 6.2c). Warm maritime air from the South Atlantic flowed onshore across Dronning Maud Land and Prydz Bay, penetrating deep into the continental interior and reaching the high plateau and Adélie Land (Fig. 6.2d). The ridge was most pronounced

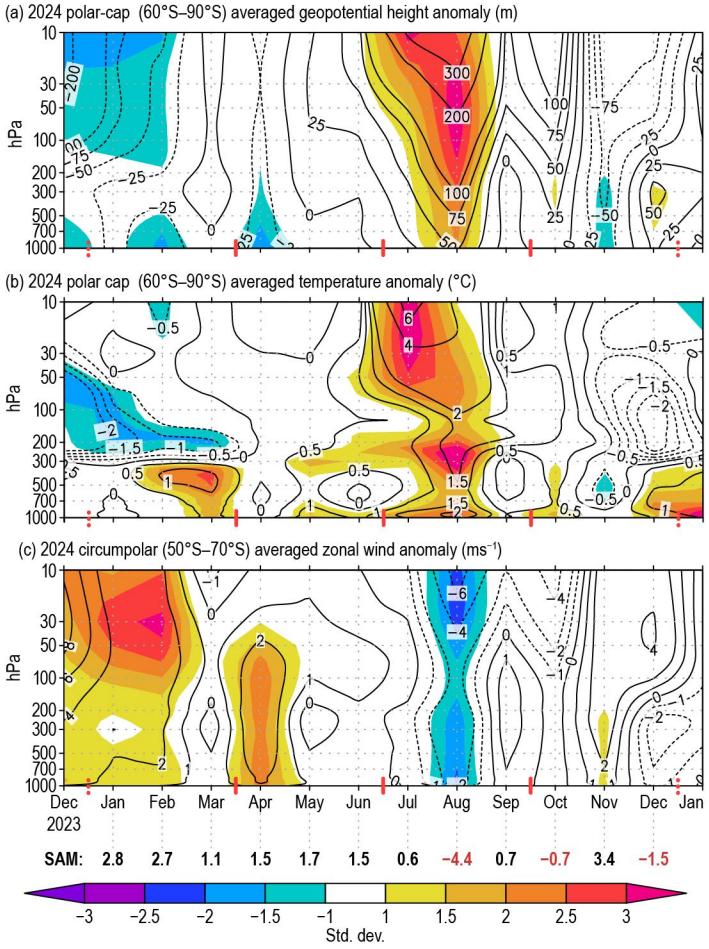

Fig. 6.3. Area-averaged (weighted by cosine of latitude) monthly anomalies over the southern polar region in 2024 relative to 1991–2020: (a) polar cap (60°S–90°S) averaged geopotential height anomalies (m; contour interval is 25 m up to ±100 m and 100 m after ±100 m); (b) polar cap averaged temperature anomalies (°C; contour interval is 0.5°C up to ±2°C and 2°C after ±2°C); (c) circumpolar (50°S–70°S) averaged zonal wind anomalies (m s^{-1}; contour interval is 2 m s^{-1} with an additional contour at ±1 m s^{-1}). Shading depicts standardized monthly anomalies as indicated by the color bar at bottom. Red vertical bars indicate the four climate periods used for compositing in Fig. 6.3; the dashed lines near Dec 2023 and Dec 2024 indicate circulation anomalies wrapping around the calendar year. Values from the Marshall (2003) Southern Annular Mode (SAM) index are shown below (c) in black (positive values) and red (negative values). (Source: ERA5)

along the coast in July, confining the warming to Dronning Maud Land but, in August, it extended poleward into East Antarctica (Fig. 6.2d), compounded by the downward propagation of positive geopotential height anomalies from the stratospheric warming (Fig. 6.3a). Notably, the SAM index reached its lowest August value since 1963, which was the second-lowest August value on record (since 1957).

Numerous monthly mean records were set in July and August. Syowa recorded its highest pressure on record in July (Fig. 6.4b) when the ridge was centered along the coast. In August, record-high pressures were reported in nearly every region of Antarctica, including Relay Station AWS on the plateau (Fig. 6.4f), Marble Point AWS on the Ross Ice Shelf (Fig. 6.4e), and Bellingshausen on the Antarctic Peninsula (not shown). There were also record-high temperatures throughout much of East Antarctica in August, with Relay Station AWS, Syowa, Mawson, and Davis all recording their warmest August on record (Fig. 6.4; Davis not shown). While weather observations are sparse over the ice sheet interior, ERA5 estimates a broad area of temperatures 6°C–10°C above average across much of the interior for the two-month period (Fig. 6.2d), consistent with available observations (Fig. 6.4). Also noteworthy was Dome C II AWS, which recorded its windiest August on record (since 1980; not shown).

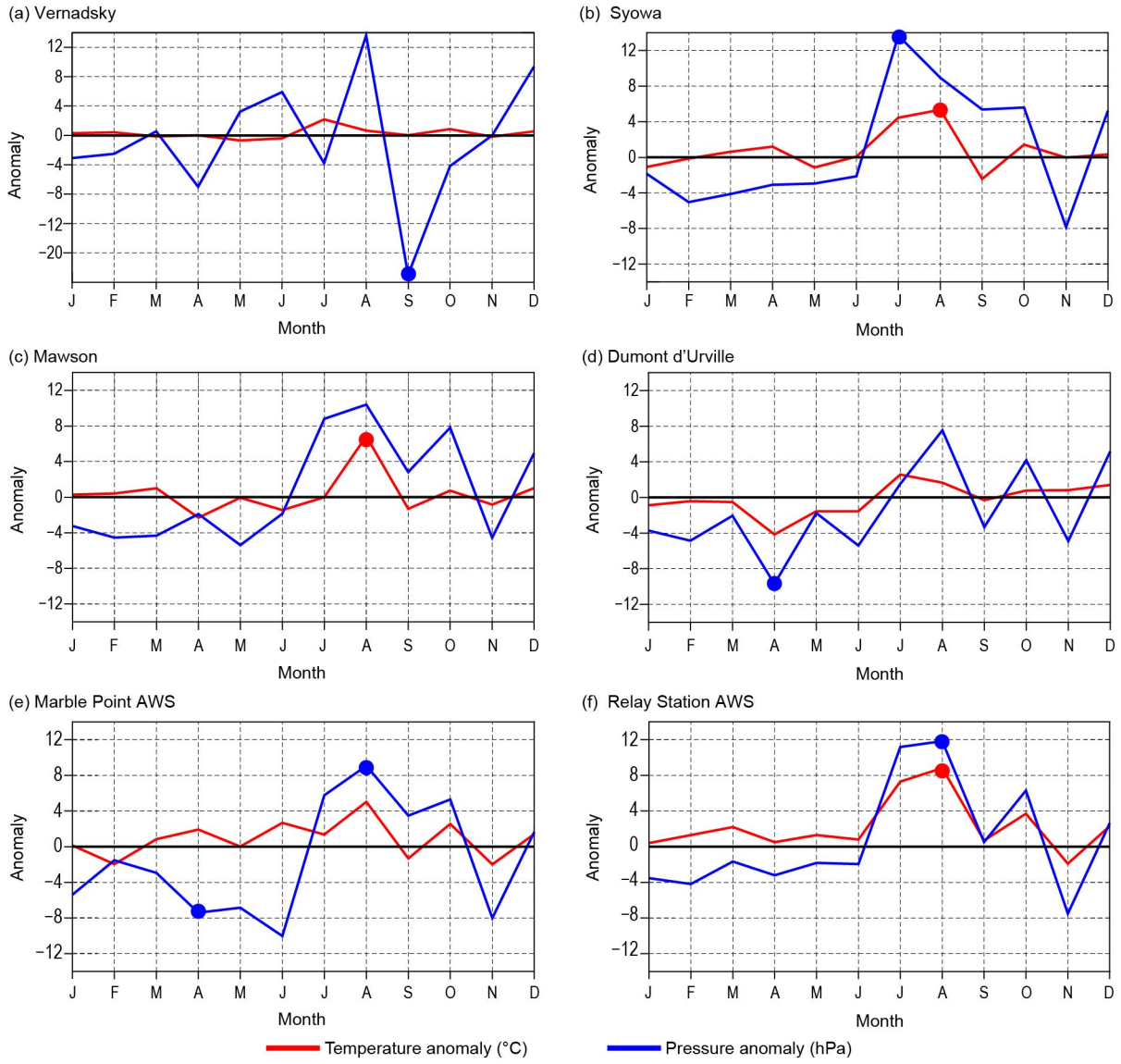

Fig. 6.4. Observed monthly Antarctic surface air temperature and station pressure anomalies during 2024 from six representative stations (four staffed [a]–[d], and two automatic [e],[f]). Anomalies for temperature (°C) are shown in red and mean sea level pressure/surface pressure (hPa) are shown in blue. Filled circles denote monthly mean records set in 2024. The station records start in 1950 for Vernadsky, 1957 for Syowa, 1954 for Mawson, 1956 for Dumont d'Urville, 1980 for Marble Point automatic weather station (AWS), and 1995 for Relay Station AWS. See Fig. 6.1 for station locations. Note the y-axis in (a) extends from +14 to –20, while all other panels range from ±14.

Pressure and temperature largely returned to average values during September and October (Figs. 6.2e,f, 6.3a,b), except for a regionally significant low-pressure system that developed over the Antarctic Peninsula in September, with Vernadsky recording pressure 20 hPa below average. Vernadsky (Fig. 6.4a), Rothera, Bellingshausen, Esperanza, and Marambio all recorded their lowest September pressure on record. Above-average surface pressure persisted over the southeast Atlantic Ocean and coastal East Antarctica. The low–high pressure couplet resulted in continued warm northerly flow and above-average temperatures over the eastern Weddell Sea and Dronning Maud Land, contributing to record-low sea ice extents in the eastern Weddell Sea during the winter of 2024 (section 6f). The cyclone also suppressed precipitation across West Antarctica, contributing to record-low SMB over the grounded ice sheet in September (section 6c).

The year concluded with a moderate (1.5 std. dev.) negative pressure anomaly over the polar cap in November followed by generally above-average pressure in December (Fig. 6.3a). November featured a pronounced positive phase of the SAM (highest SAM index value of the year: +3.4) with intensified circumpolar westerlies and below-average temperatures over the polar cap (Figs. 6.3b,c). The Ross Ice Shelf region saw record-low November pressures at Ferrell AWS and Gill AWS (not shown). December was relatively calm (not shown), with generally above-average temperatures and near-average pressure, except for a strong ridge of high pressure (>2 std. dev.) over the Antarctic Peninsula and Weddell Sea, which led to anomalously warm conditions in West Antarctica.

c. Ice sheet surface mass balance

—L. Trusel, M. Maclennan, R. Baiman, M. Bahrami, C. Kittel, R. Tri Datta, and C. Amory

Surface mass balance (SMB) represents the net effect of all processes that add or remove mass from the surface of an ice sheet. For the Antarctic Ice Sheet (AIS), snowfall is the primary SMB contributor, delivering ~2300 Gt annually (van Wessem et al. 2018; Agosta et al. 2019; Mottram et al. 2021). Sublimation represents the largest negative term in the AIS SMB, given that most surface melt refreezes within the firn (Mottram et al. 2021). Strong SMB gradients exist spatially (Fig. 6.5a), with high relief coastal areas receiving >500 mm water equivalent (w.e.) yr^{-1} compared to <50 mm w.e. yr^{-1} across the high-elevation plateau of East Antarctica. Strong seasonal variability likewise exists, with the largest mass gains occurring in austral autumn (March–May) and the least in austral summer (December–February; Fig. 6.6a). Although only SMB on grounded ice directly affects sea level, SMB on floating ice shelves is critical for maintaining firn layer health and ice shelf stability (The Firn Symposium Team 2024). Typically, high-magnitude extreme precipitation events (EPEs) delivered by atmospheric rivers (ARs) drive AIS SMB gains (Turner et al. 2019; Wille et al. 2021; Maclennan et al. 2022), while reduced AR activity can lead to anomalously low snowfall and a more negative mass balance (Davison et al. 2023). Sea ice can also play an influential role in SMB by modulating the amount and extent of moisture transport over the ice sheet (Wang et al. 2020; Trusel et al. 2023; Hanna et al. 2024; Kolbe et al. 2025).

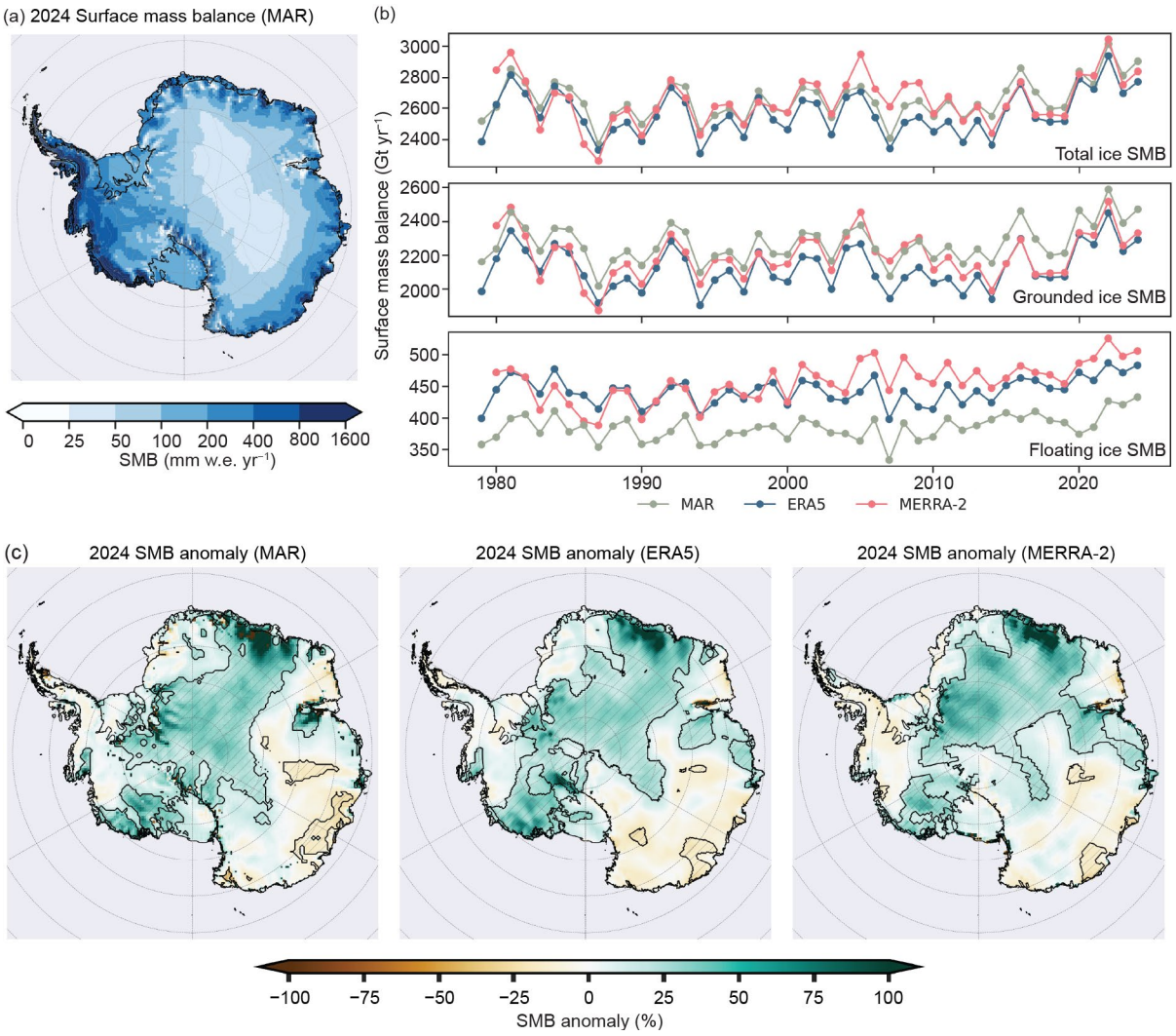

Fig. 6.5. (a) Model for Surface Mass Balance of the Arctic Ice Sheets (MAR) 2024 surface mass balance (SMB; mm water equivalent [w.e.] yr^{-1}). (b) Time series of SMB in Gt (10^{12} kg) yr^{-1} over the full ice sheet and its grounded and floating portions. (c) Annual MAR, ERA5, and MERRA-2 SMB anomalies for 2024 relative to the 1991–2020 mean (%). The 2024 SMB anomalies are higher than the 1991–2020 standard deviation of the respective datasets in the hatched areas outlined in black.

Here, we estimate the 2024 SMB as total precipitation minus evaporation and sublimation (P–E) using ERA5 (Hersbach et al. 2020) and MERRA-2 (Gelaro et al. 2017) reanalyses, following recent studies (e.g., Medley and Thomas 2019; Lenaerts et al. 2019). Though important biases remain, particularly regarding ice sheet–cloud–radiation feedbacks and precipitation,

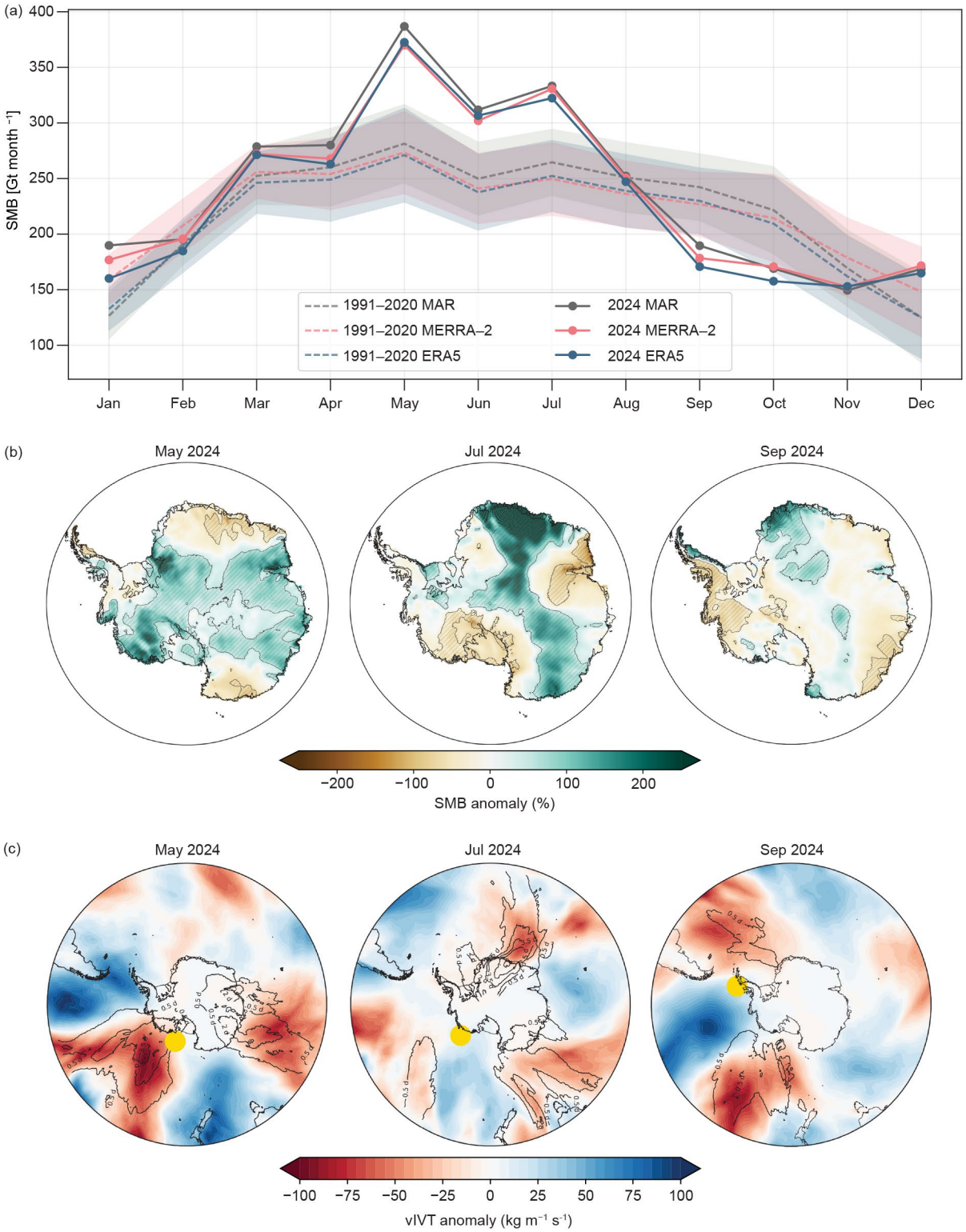

Fig. 6.6. (a) Monthly cycle of (grounded and floating) Antarctic Ice Sheet surface mass balance (SMB) in Gt month^{-1} for MERRA-2 (pink), ERA5 (blue), and the Model for Surface Mass Balance of the Arctic Ice Sheets (MAR; gray). The 2024 values are shown with a solid line and the 1991–2020 average is shown in a dotted line; 1 std. dev. is shaded. (b) Monthly SMB anomalies (ERA5), with hatched regions indicating anomalies exceeding 1 std. dev. relative to the 1991–2020 average. (c) Anomalies in ERA5 meridional integrated vapor transport (vIVT) with negative values (reds) indicating enhanced moisture transport toward Antarctica, contours representing the number of days featuring atmospheric rivers detected in MERRA-2, and yellow dot representing the monthly mean Amundsen Sea Low center following Hosking et al. (2014).

evaluations of both reanalyses indicate that they reliably represent recent Antarctic climate (Gossart et al. 2019; Medley and Thomas 2019; Wang et al. 2016). SMB was also assessed using the polar-oriented regional climate model Model for Surface Mass Balance of the Arctic Ice Sheets (MAR) forced by ERA5, which explicitly represents ice sheet SMB processes, including firn evolution and meltwater runoff (Kittel et al. 2021). ERA5 offers the highest resolution (0.25°), followed by MAR (35 km) and MERRA-2 (0.625° × 0.5°). While ERA5 and MAR extend back to 1979, MERRA-2 begins in 1980. To ensure spatial consistency, each dataset was bilinearly regridded to the ERA5 grid before masking with grounded and floating ice extents from the Antarctic Digital Database (Gerrish et al. 2023). Annual and monthly anomalies in SMB and vector-invariant water transport (vIVT) are compared to 1991–2020 climatologies and we detect ARs in MERRA-2 using an approach adapted from Wille et al. (2021).

In 2024, the grounded AIS SMB equaled 2291 Gt (ERA5), 2333 Gt (MERRA-2), and 2472 Gt (MAR), representing anomalies of 1.2 to 1.7 std. devs. above the 1991–2020 climatological means (ERA5: 2104±109 Gt yr^{-1}; MERRA-2: 2186±106 Gt yr^{-1}; MAR: 2254±97 Gt yr^{-1}). These results were the second highest on record in MAR (behind only 2022), fifth highest in ERA5, and sixth in MERRA-2. Considering floating ice shelves alone, 2024 ranked as the highest on record in MAR and second highest in ERA5 and MERRA-2. Despite elevated SMB in 2024 and other recent years, no significant trend ($p \leq 0.01$) was detected for total or grounded SMB, although significant positive trends exist across the AIS's floating ice shelves in MAR (0.6 Gt yr^{-1}) and MERRA-2 (1.5 Gt yr^{-1}).

Examination of SMB across months further highlights the exceptional conditions in 2024. May emerged as the most anomalous month of the year (Fig. 6.6a) and ranked among the snowiest on record over the full ice sheet (first, second, and third in MAR, MERRA-2, and ERA5, respectively). Heavy gains in May more than offset the largely typical low SMB observed from January through April, yielding the highest cumulative SMB on record from May to August according to ERA5, before below-average precipitation during September–November ultimately reduced the cumulative SMB anomaly. The positive SMB anomalies in May were widespread, with much of East and West Antarctica experiencing significant mass gains (Fig. 6.6b). This pattern aligned with positive anomalies in southward vIVT and AR activity that funneled moisture from lower latitudes into the Ross–Amundsen and Wilkes Land sectors (Fig. 6.6c). Moreover, moisture transport toward West Antarctica passed over regions exhibiting sea surface temperature anomalies exceeding 2°C in the South Pacific Ocean (section 6g) and reduced sea ice in the Ross–Amundsen Sea (not shown; section 6f), conditions that likely contributed to enhanced SMB. The widespread but generally low-magnitude, positive SMB anomalies of May contrast to the high localized SMB conditions in July, when particularly strong SMB increases in Dronning Maud Land were driven by focused ARs (Fig. 6.6) on the western side of a strong ridge of high pressure (section 6c).

In contrast, September was the driest on record over the grounded ice sheet in all datasets assessed, driven by an acute shortfall of precipitation across West Antarctica (Fig. 6.6b). Typically, 6.5±0.8 Gt day^{-1} of snowfall occurs in September according to MERRA-2 climatology, yet 2024 averaged only 4.9 Gt day^{-1}, largely due to an absence of EPEs. Normally, days in the top 15% of snowfall contribute 78±41 Gt (38% of total September snowfall), but no days in September 2024 featured snowfall in the top 15% of daily precipitation. Antarctic EPEs are often associated with elevated vIVT anomalies and ARs (Turner et al. 2019; Wille et al. 2021; Maclennan et al. 2022), however, in September 2024, few ARs with high vIVT reached the continent and instead were concentrated equatorward over the Amundsen Sea (Fig. 6.6c). A likely driver of this lack of snowfall and landfalling ARs was the extreme eastward position of the Amundsen Sea Low (see Fig. 6.2e)—farther east than any September since 1959 according to the approach of Hosking et al. (2016)—which acted to suppress moisture transport toward West Antarctica and contributed to the extreme low SMB.

d. Ice sheet seasonal melt extent and duration

—M. MacFerrin, T. Mote, A. F. Banwell, and T. Scambos

Surface melt on the Antarctic Ice Sheet (AIS) occurs primarily on the low-elevation coastal margins, especially on the Antarctic Peninsula and on the ice shelves surrounding the continent. It plays a small role in the total mass balance of the AIS relative to far larger contributions from snow accumulation, glacier calving, and basal melting. However, surface melting is a key measure of ice sheet and ice shelf stability. As meltwater percolates and re-freezes, it increases the density of the underlying firn, and if melt volume is sufficient, the accumulated meltwater can induce ice shelf break up (Banwell et al. 2013) and glacier acceleration through hydrofracture (Scambos et al. 2014). This section focuses on the melt season spanning 1 October 2023 through 30 April 2024. The 2024/25 Antarctic melt season will be discussed in next year's report.

Daily surface melt is mapped using satellite-derived passive-microwave brightness temperatures. The source data are distributed as daily composited polar stereographic brightness temperatures by the National Snow and Ice Data Center (NSIDC; products NSIDC-0001, Meier et al. 2019 and NSIDC-0007, Gloerson 2006) spanning 1979 through the present day. Daily passive microwave brightness temperatures using the 37-GHz horizontal polarization as well as the 37- and 19-GHz vertical polarization channels have been acquired by the Scanning Multichannel Microwave Radiometer (SMMR), Special Sensor Microwave Imager (SSM/I), and Special Sensor Microwave Imager Sounder (SSMIS) sensors aboard the NOAA Nimbus-7 and Defense Meteorological Satellite Program (DMSP) F8, F11, F13, F17, and F18 satellites. The austral melt season is defined here as 1 October through 30 April. Although small brief melt events can be measured along Antarctica's coastal margins throughout the year and even during the austral winter, the vast majority of melt happens during these seven months, with most melt typically occurring in December and January. An ice extent mask of 25-km grid cells for the AIS was developed from the Quantarctica v3.0 Detailed Basemap dataset (Norwegian Polar Institute 2018). All 25-km cells that contain ≥50% land ice or ice shelf are included. We divide the AIS into seven melt extent and climate regions by clustering glaciological drainage basins (based on The IMBIE Team 2019; Fig. 6.7b). Melt is determined by 37-GHz horizontally polarized brightness

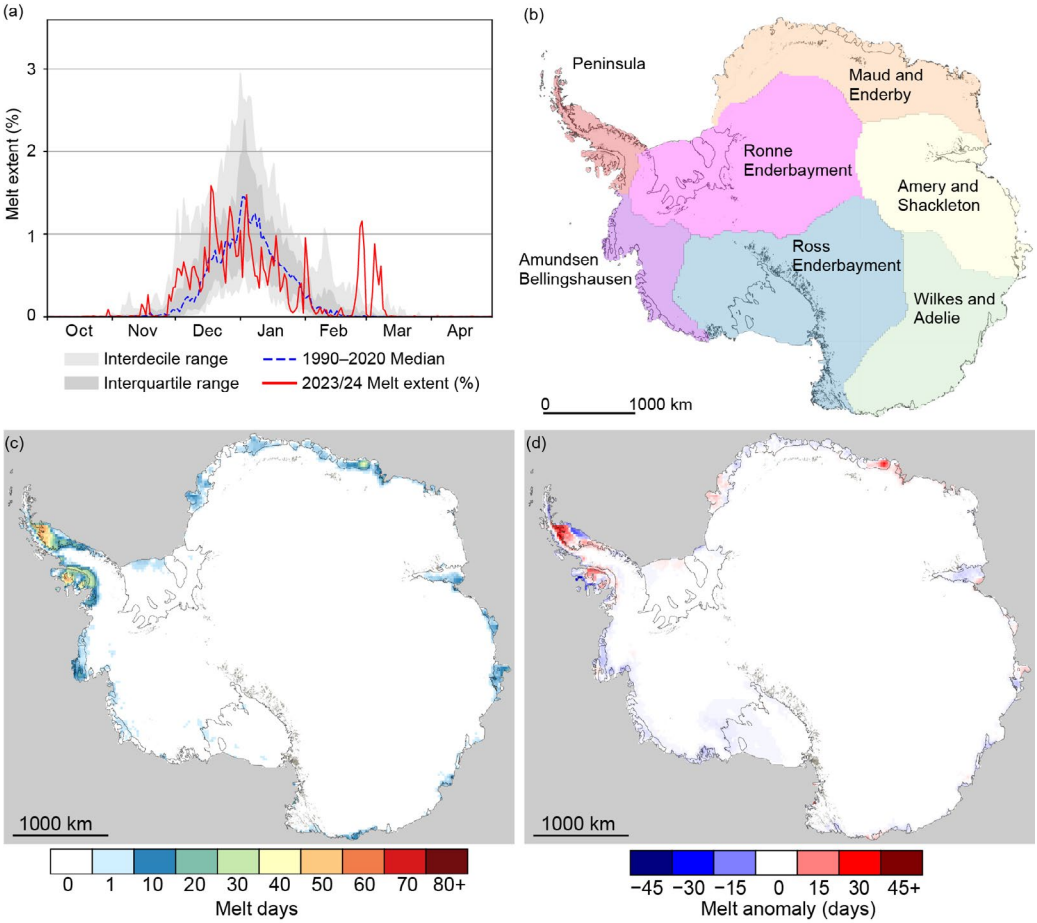

Fig. 6.7. (a) Daily surface melt extent (%; from National Snow and Ice Data Center [NSIDC]-0001, 0007) across the Antarctic Ice Sheet for the 2023/24 melt season, with 1990–2020 median values in blue and interdecile and interquartile ranges shaded in gray. (b) Reference map of Antarctic melt analysis regions, including the two shown in Fig. 6.8. (c) Map of the sum of melt days across the Antarctic Ice Sheet. (d) Map of the anomaly of the sum of melt days compared to mean values from the 1990–2020 reference period.

temperatures that exceed a dynamically established threshold each season from a simple microwave emission model that would be expected in the presence of liquid water in near-surface layers of ice and snowpack. The method used here was first developed to track the Greenland Ice Sheet's surface melt (Mote and Anderson 1995; Mote 2007, 2014). Large seasonal fluctuations in passive microwave emissions from some areas of dry polar firn in Antarctica can create false positive melt indications in an unmodified version of the Greenland algorithm. This was mitigated by filtering areas that only marginally exceed the melt threshold (<10K) in the 37-GHz horizontal polarization in regions with a negative 18/19-GHz minus 37-GHz frequency gradient in the vertical polarization, which has been used in previous season reports of Antarctic melt (MacFerrin et al. 2021, 2022, 2023).

According to passive-microwave satellite observations, the 2023/24 melt season recorded an overall below-average cumulative melt index (days · area) of 6.90 million km^2-days; this was about 8.6% below the median melt index of 7.55 million km^2-days during the 1990–2020 baseline period (Fig. 6.7). However, the 2023/24 melt season was punctuated by substantial spatial and temporal positive and negative anomalies in individual regions.

The Antarctic Peninsula (Figs. 6.8a,c) saw an annual melt index of 4.72 million km^2-days, 10.2% above the baseline mean value of 4.28 million km^2-days. Melt in the Peninsula was strongly affected by significant melting in late December and early January, followed by two widespread melt events in late February and early March that resulted in the northern Larsen C Ice Shelf having up to 30 days more melt than the baseline 1990–2020 median. Those late-season melt periods (28–29 February and 4–8 March 2024) broke previous daily records for areal melt extents

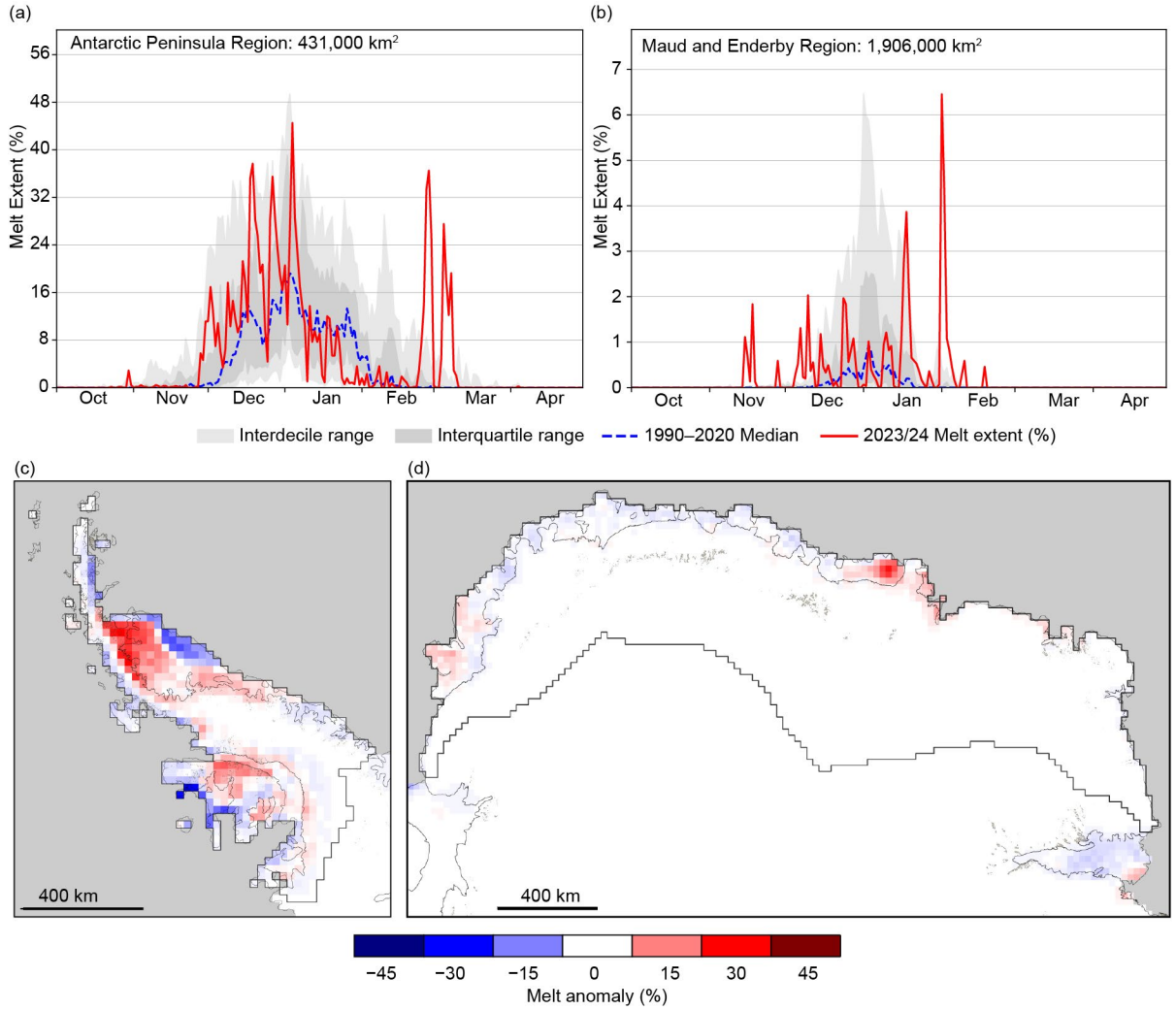

Fig. 6.8. (a),(b) Daily 2023/24 melt extent (%; from National Snow and Ice Data Center [NSIDC]-0001, 0007) over (a) the Antarctic Peninsula region and (b) the Dronning Maud Land and Enderby Land region. (c),(d) Maps of 2023/24 melt anomalies (days) over (c) the Antarctic Peninsula region and (d) the Dronning Maud Land and Enderby Land region.

in the satellite record since 1979, both for the Antarctic Peninsula and the continent as a whole (which is dominated by Peninsula melt; see https://nsidc.org/ice-sheets-today for details on this event).

Like the Peninsula, the Dronning Maud and Enderby Land region of Antarctica also displayed a higher-than-average melt season (Figs. 6.8b,d), recording a total melt index 24.5% more than the baseline period, with several substantial melt events from mid-November through mid-February. The Maud and Enderby region experienced a pair of relatively extensive melt events on 1 February and 18 February 2024 that broke the previous daily records for that region. Melt extent there was concentrated on the Standcomb–Brunt and Riiser–Larsen ice shelves on the eastern side of the region, and the Baudouin and Prince Harald ice shelves on the western side. Portions of the Baudouin Ice Shelf, in particular, experienced more than 30 days melt duration in excess of a median year (Fig. 6.8d).

All other regions of Antarctica experienced a melt index in 2023/24 that was lower than their baseline values, contributing to a relatively modest (8.6% below-average) melt index for the Antarctic continent.

e. Ice sheet mass balance

—S. Adusumilli and H. A. Fricker

The Antarctic Ice Sheet (AIS) stores 58 m of global sea level equivalent. AIS mass balance is the difference between mass gained through accumulation (snowfall minus sublimation) at the surface across the continent and mass lost around margins where ice is delivered to the ocean through its floating ice shelves. For any given time period, the net mass balance for the grounded AIS is the difference between competing processes (mass gain from accumulation and mass loss from dynamic thinning), which depends on the integrated effects of interactions between the ice, ocean, and atmosphere (e.g., Smith et al. 2020). Since 1992, the AIS has experienced overall net mass loss of grounded ice (Otosaka et al. 2023), dominated by trends in the West Antarctic Ice Sheet (WAIS), and its contribution has increased, reaching 0.32 mm of sea level rise per year between 2017 and 2020.

Three complementary techniques track grounded AIS mass changes: 1) satellite altimetry, with elevation changes combined with a firn density model; 2) mass fluxes from synthetic aperture radar (SAR) ice flow rates, ice thickness, and climate models; and 3) gravimetry (e.g., Gravity Recovery and Climate Experiment [GRACE], only for grounded ice). The European Space Agency (ESA)/NASA Ice Mass Balance Intercomparison Exercise (IMBIE) combines all three methods for robust mass change assessments (Otosaka et al. 2023). At the time of writing, there were no published estimates of total AIS mass or height change for 2024. Hence, two different techniques are used: techniques: ICESat-2 satellite laser altimetry and GRACE/GRACE Follow-On (GRACE-FO). Only grounded ice changes are considered, as altimetry-derived height changes over ice shelves at sub-annual time scales are noisy and require further processing, and gravimetry cannot detect mass changes on floating ice.

Following the same approach as used for previous years of this report (e.g., Clem et al. 2023, 2024), estimates of height changes over the grounded ice sheet were derived from NASA's ICESat-2 laser altimeter using all available data for 2024 (until 7 November 2024). The ATLAS/ICESat-2 L3B Slope-Corrected Land Ice Height Time Series, version 6 (Smith et al. 2022), which provides precise estimates of height along repeated ground tracks at 60-m along-track resolution, was used. Along-track height changes between the available data in Cycle 25 (centered around November 2024) and the corresponding data from Cycle 21 (centered around November 2023; Fig. 6.9) were derived. To analyze seasonal variability, height changes over three-month intervals between successive ICESat-2 data acquisition cycles during the November 2023 to November 2024 period (Fig. 6.10) were also derived. The final height change maps were smoothed using a Gaussian filter with a 30-km diameter.

Annual mass anomalies derived from NASA's satellite gravimeter (GRACE-FO; Fig. 6.9b) for 2024 were calculated. Data from the Jet Propulsion Laboratory GRACE and GRACE-FO Ocean, Ice, and Hydrology Equivalent Water Height Coastal Resolution Improvement (CRI) Filtered

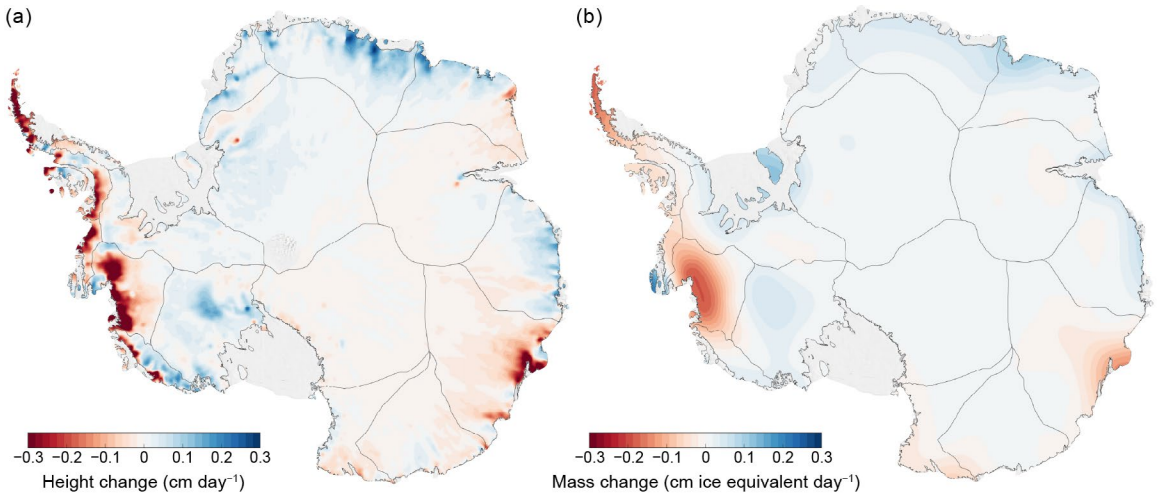

Fig. 6.9. Annual change maps for the Antarctic Ice Sheet from Nov 2023 to Nov 2024. (a) Height change from ICESat-2 (cm day^{-1}); and (b) ice equivalent mass change from Gravity Recovery and Climate Experiment Follow-On (GRACE-FO) (cm ice equivalent day^{-1}).

Release 06 version 02 "mascon data" was used. Mascons (or mass concentration blocks) are 3° × 3° spherical caps placed on an elliptical approximation of Earth's surface over which these data are provided (Wiese et al. 2023a). Gravity-derived mass anomalies were calculated for approximately the same period as used for ICESat-2 (November 2023 to November 2024), with the same three-month averaging. To determine ice sheet mass anomalies, all mascons containing more than 10,000 km^2 of land were identified, according to the provided CRI land mask. The area-averaged rates of change were interpolated using bilinear interpolation according to the location of the geometric center of the land area contained within the mascon. All non-land areas were then masked using the Bedmachine ice mask (Morlighem et al. 2020). Time series of mass changes integrated over the ice sheet (Fig. 6.11) from the Level 4 Antarctica Mass Anomaly Time Series data product (Wiese et al. 2023b) were also retrieved.

The maps of annual change in ice sheet height for November 2023 to November 2024 from ICESat-2 (Fig. 6.9a) and mass from GRACE-FO (Fig. 6.9b) show ongoing losses of ice in the Amundsen Sea sector of WAIS, where losses have been observed since 1992 (e.g., Smith et al. 2020; Clem et al. 2022). Continued ice loss is occurring in the Antarctic Peninsula, particularly the outlet glaciers north of central Larsen C and in the Bellingshausen Sea. In East Antarctica, continued losses at Totten Glacier are found throughout the record (Fig. 6.9b), as well as increases in snowfall/height in the Dronning Maud Land region (Fig.6.9a), especially during August to November 2024 (Fig. 6.10d).

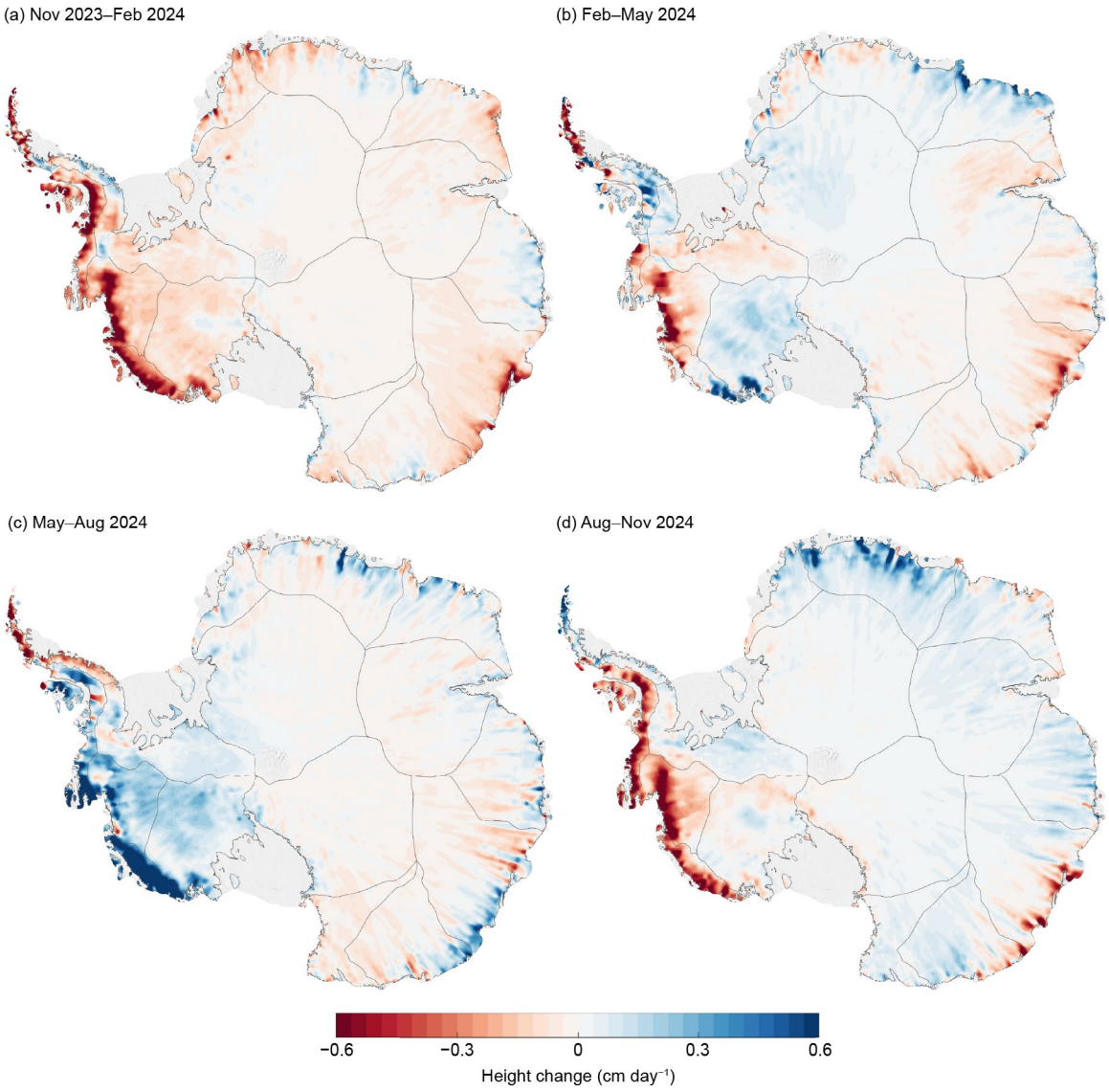

Fig. 6.10. Maps of height change from ICESat-2 shown at three-month intervals for (a) Nov 2023–Feb 2024, (b) Feb–May 2024, (c) May–Aug 2024, and (d) Aug–Nov 2024. Dates represent the central month of each three-month ICESat-2 data acquisition cycle.

The GRACE-FO data show a net mass loss over AIS between January and November 2024 of 125 Gt, which was slightly higher than the average annual mass loss of 100 Gt yr^{-1} between 2003 and 2023 (Fig. 6.11). Mass changes are on a similar trajectory to those in 2023 and reflect continued mass loss since the record-breaking 298 Gt mass gain that occurred in 2022. The ICESat-2 three-monthly maps (Fig. 6.10) enable the constraint of the timing of some of these larger mass fluctuations. For example, they reveal that temporal mass gains in 2023 were in part due to snow accumulation across Dronning Maud Land and a large signal in the Amundsen Sea sector and on the Siple Coast in May to August 2024, which although much lower in density, offset some of the large mass losses in coastal WAIS.

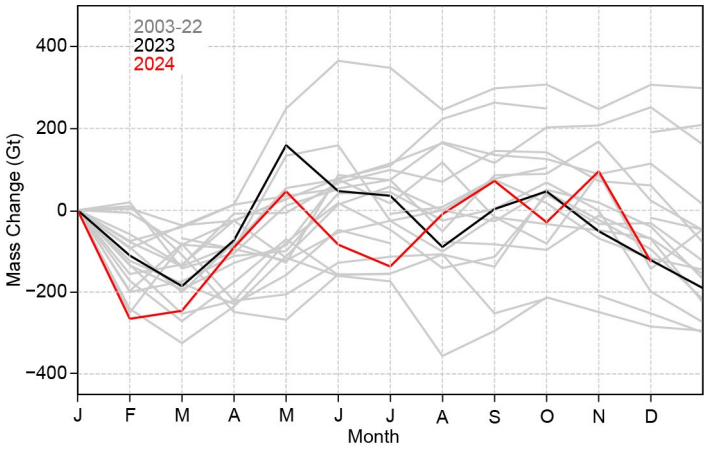

Fig. 6.11. Annual mass change (Gt) from Gravity Recovery and Climate Experiment (GRACE) and GRACE Follow-On (GRACE-FO). Time series of monthly mass changes from GRACE and GRACE-FO, with 2023 and 2024 highlighted by the black and red line, respectively.

f. Sea ice extent, concentration, and seasonality

—P. Reid, S. Stammerjohn, R. A. Massom, S. Barreira, T. Scambos, and J. L. Lieser

Antarctic sea ice—formed from the freezing of the ocean surface—is a critical component of Earth's climate system and biophysical environment, and performs the following functions: moderates solar heating of the ocean and the global energy budget by strongly reflecting incoming solar radiation (Riihelä et al. 2021); modulates ocean–atmosphere interactions (Josey et al. 2024); contributes to the global ocean circulation (Meredith and Brandon 2017); protects ice shelves from potentially destructive wave action (Massom et al. 2018); and serves as a key habitat for a plethora of polar species that are highly adapted to (and dependent on) its presence and seasonal rhythms (Thomas 2017).

Throughout most of 2024, both the net sea ice extent (SIE) and sea ice area (SIA—the product of sea ice extent and concentration) remained well below average or at record-low levels for the satellite time series from 1979 onwards (Fig. 6.12a). However, sea ice coverage rebounded to near-average values towards late December. The record for monthly mean low SIE for November set in 2023 (Reid et al. 2024) was broken in 2024, and several daily record lows were recorded in early September and mid-November (a number of days of record-low SIA also occurred through July to November). Antarctic coastal exposure (Reid and Massom 2022) was at record-breaking high daily values through much of January and February, at times more than twice the long-term (1991–2020) average. Similarly, the areal extent of summertime fast ice (Fraser et al. 2023) crashed to a record low (since its analysis started in 2000) during 2024. Annual daily minimum of both net SIE and SIA was recorded on 18 February (1.97×10^6 km^2 and 1.40×10^6 km^2, respectively); they were, respectively, third and second lowest on record. Annual daily maximum values of net SIE and SIA were recorded on 30 and 21 September, respectively (17.18×10^6 km^2 and 13.55×10^6 km^2), with both being the second lowest on record (behind 2023; Reid et al. 2024).

The well-below-average SIE observed in 2024 marks a continuation of the pattern of low and record-low coverage since 2016. In particular, and as with 2023 (Reid et al. 2024), overall sea ice seasonal growth in 2024 lagged well behind the long-term mean during the autumn–winter advance phase. Changes in upper-ocean conditions may be largely responsible for the increasing persistence in negative Antarctic SIE anomalies and reduced duration observed since 2016 (Cheng et al. 2022; Purich and Doddridge 2023; Raphael et al. 2025). However, the net values of SIE do not capture important regional and seasonal variations, which are outlined below.

In the lead-up to 2024 (October through December 2023), a deep Amundsen Sea Low and a general contraction of circumpolar lows enhanced northward advection of sea ice within the Ross, Amundsen, and Bellingshausen Seas to warmer waters. This led to an unusually early sea ice retreat for 2023/24, and a near-record annual daily SIE minimum that was marginally greater than the previous two summers. From January through March, Antarctic SIE was substantially below average around most of the continent, except for parts of the Amundsen, western Ross, and Weddell Seas, where SIE was slightly above average (Fig. 6.12b); sea ice concentration was anomalously high in the central Weddell Sea (Fig. 6.12c).

Sea ice conditions changed abruptly in April, when development of a zonal wave-3 atmospheric pattern (section 6b) retarded sea ice growth and advection to the east of the central low-pressure systems (~60°E, 150°E, and 60°W) while enhancing SIE to the west. As a result, SIE from April through August remained substantially below average in the Ross and eastern Weddell Seas and across much of the western Pacific (Fig. 6.12b). These regions of relatively low SIE also coincided with regions of high SST (section 6g). In particular, SIE in the eastern Weddell Sea (~10°W–60°E) was greater than five standard deviations below average. Lower sea ice growth in this region was likely influenced by a diminished Winter Water layer—a cold subsurface layer that is a remnant of the previous winter's mixed layer capped by seasonal warming and freshening (see Park et al. 1998; Sabu et al. 2020; Spira et al. 2024)—and enhanced vertical mixing of warmer waters from below. This is somewhat supported by the enhanced ocean–atmosphere heat flux in the Atlantic region of the Southern Ocean in August (Fig. 6.14d). Moreover, the stratospheric warming event in July (sections 6b, 6h) likely contributed to the substantial reductions in SIE (Fig. 6.12b) by increasing monthly averaged near-surface air temperatures across the sea ice zone off Dronning Maud Land (~15°E–30°E) by ~10°C during July–August (section 6b). Sea ice coverage in the eastern Weddell Sea remained much lower than average through to the end of

the year. Conversely, there was a significant expansion of sea ice across the western Pacific and western Ross Sea (~110°E–180°E) and in the Amundsen–Bellingshausen and western Weddell Seas between April and June. This sea ice advance continued in the western Weddell Sea and was particularly rapid in August (Fig. 6.12b); SIE values there exceeded four standard deviations above average, likely due to persistent cold southerly winds beginning in May. A similar albeit less pronounced rapid sea ice advance occurred in the western Ross Sea during early August. The sudden sea ice expansion within these two regions is reflected in the net SIE graph (Fig. 6.12a).

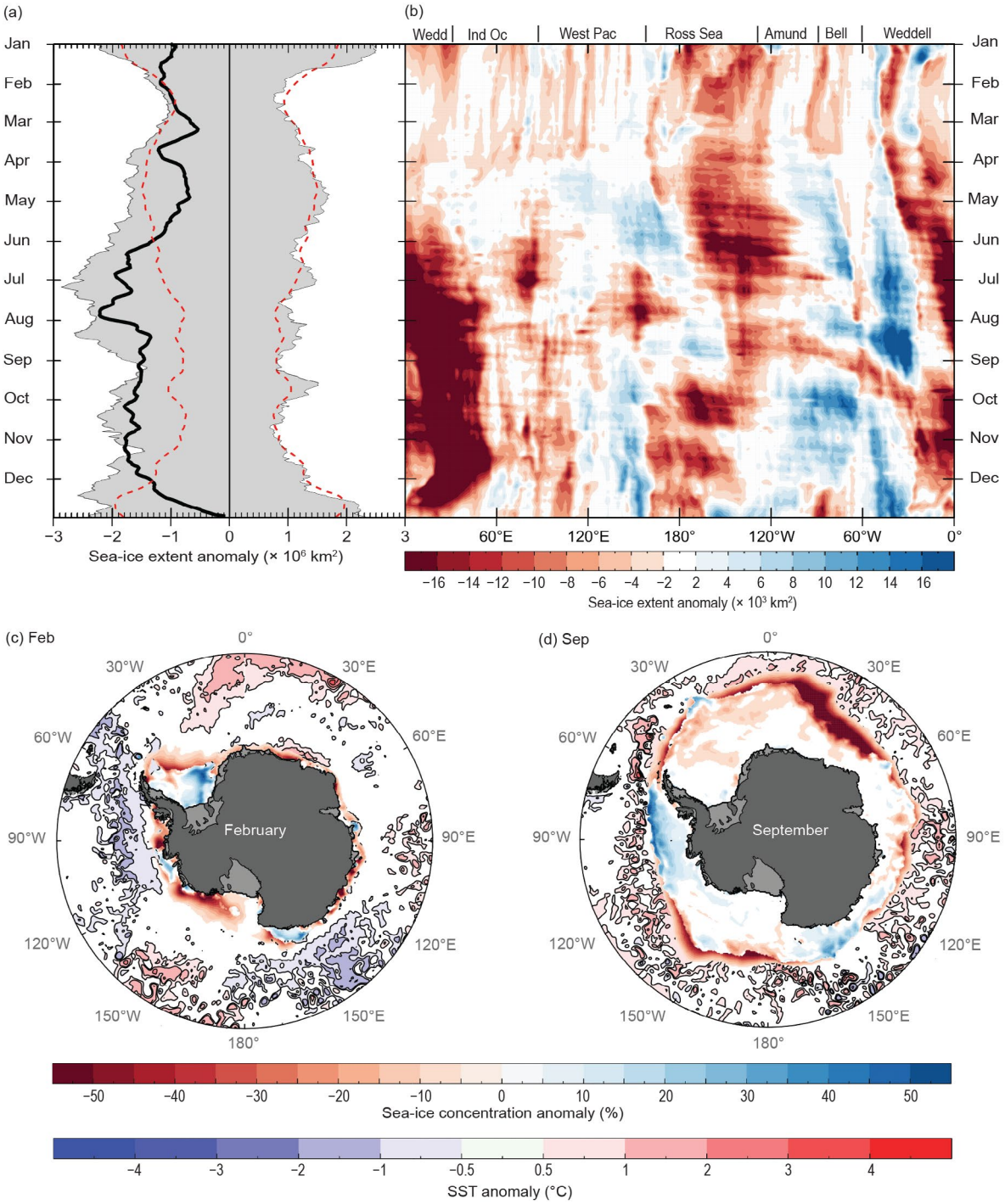

Fig. 6.12. (a) Time series of net daily sea ice extent (SIE) anomalies for 2024 (solid black line; based on a 1991–2020 climatology). Gray shading represents historical (1979–2023) daily SIE anomalies, red dashed line represents ±2 std. dev., and (b) Hovmöller (time–longitude) representation of daily SIE anomaly (× 10³ km² per degree of longitude) for 2024. Maps of sea ice concentration anomaly (%) and sea surface temperature (SST) anomaly (°C; Huang et al. 2021) for (c) Feb 2024 and (d) Sep 2024. Sea ice concentration is based on satellite passive-microwave ice concentration data (Cavalieri et al. 1996, updated yearly for climatology; Maslanik and Stroeve 1999 for the 2024 sea ice concentration). See Fig. 6.1 for relevant place names.

Regional patterns of sea ice coverage changed again in September in response to a marked shift in large-scale atmospheric circulation (section 6b). The formation of the deep low-pressure anomaly over the Antarctic Peninsula and the southwestern Pacific (~150°E) combined with high-pressure systems over the eastern Ross and eastern Weddell Seas (Fig. 6.2e) ushered warmer northerly winds and surface waters into the Ross and western Weddell regions to reduce sea ice coverage there. In the Bellingshausen and Amundsen Seas, as well as north of Victoria Land at ~150°E (Fig. 6.12d), a late surge in seasonal sea ice growth reversed the early September record lows, producing a late annual daily SIE maximum. This positive SIE anomaly in the Amundsen–Bellingshausen Seas intensified in October and persisted into December (Fig. 6.12b).

During November and early December, regional sea ice coverage was strongly influenced by a southward contraction of the circumpolar westerlies associated with the strongly positive Southern Annular Mode (SAM) phase (section 6b), followed by a northward expansion of the westerlies (reflecting a negative SAM) in late December (section 6b). These shifts led to a lack of storm activity along the sea ice edge, which was not conducive to broad-scale sea ice retreat. Although net SIE briefly reached record-low values in early November, it was close to average by the end of December (Fig. 6.12a). This net average, however, comprises the sum of distinctly different regional components (Fig. 6.12b). Notably, the eastern Weddell Sea continued to exhibit greatly reduced sea ice cover (a pattern that began in May) and early annual retreat, along with parts of East Antarctica (~90°E–110°E), the Ross Sea (~160°E–190°W), and the Bellingshausen Sea in late December. Elsewhere, SIE remained above average, most notably in the western part of the western Pacific sector, the western Ross Sea, and the western Weddell Sea (Fig. 6.12b).

In parallel with SIE and SIA, the timings of annual sea ice advance and retreat, and resultant duration of coverage (where a sea ice year here is mid-February 2024 to mid-February 2025 [Stammerjohn et al. 2008]), show distinct regional anomalies (Fig. 6.13) that mirror those of the SIE and SIA records for 2024 (Fig. 6.12b). Annual sea ice advance was delayed by 30 days–60 days (compared to the 1991/92–2020/21 mean) across extensive tracts of the central Weddell Sea, extending eastwards across the Indian and western Pacific Ocean sectors, and the central Ross Sea through the Amundsen Sea (Fig. 6.13a). In contrast, advance was as much as 30 days–60 days earlier in the northwestern Weddell Sea, the western Antarctic Peninsula region, and across an inner band off East Antarctica (east of ~90°E–~170°W; Fig. 6.13a). The retreat pattern was patchier but mostly aligned with the advance pattern, with the

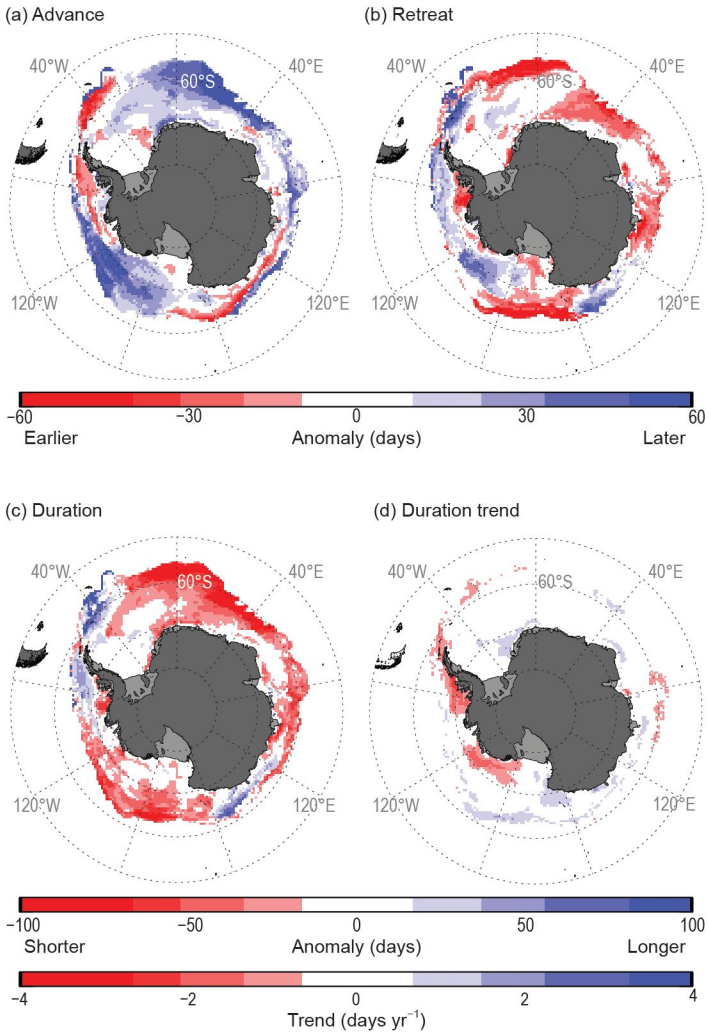

Fig. 6.13. Maps of seasonal sea ice anomaly (days) in 2024 during (a) autumn ice-edge advance, (b) spring ice-edge retreat, and (c) winter ice season duration; together with (d) winter ice season duration trend (days yr^{-1}; Stammerjohn et al. 2008). The seasonal anomalies (a)–(c) are computed against the 1991/92–2020/21 climatology; the trend (d) is computed over 1979/80–2024/25. The climatology (for computing the anomalies) is based on data from Comiso (2017; updated yearly), while the 2024/25 ice-edge retreat duration-year data are from the NASA Team Near-Real-Time Defense Meteorological Satellite Program Special Sensor Microwave Imager Sounder Daily Polar Gridded Sea Ice Concentrations (NRTSI) dataset (Maslanik and Stroeve 1999); the trend is based on the merged dataset containing 1979–2023 data from Comiso (2017) and 2024/25 data from the NASA Team NRTSI dataset (Maslanik and Stroeve 1999).

retreat being earlier (later) by 30 days–60 days where the advance was later (earlier) by 30 days–60 days. The exception was the eastern Ross Sea and outer Amundsen Sea, where the advance and retreat were both later. Seasonality maps show the marked passage of Iceberg A23a (Figs. 6.13a–c; see Sidebar 6.1). Studies have suggested an increase in sea ice concentration and thickness due to iceberg melt, so it is possible that A23a is having an influence (Merino et al. 2016; Haid et al. 2017), although analysis around Iceberg A68 (Meredith et al. 2023) suggests this to be quite localized.

The continuation during 2024 of the recent (post-2016) reduced net sea ice coverage provides further observational support of a transformation in the atmosphere–ocean–sea ice interaction system, which points to an overall decline in sea ice due to a warmer global climate.

Sidebar 6.1: How to train your iceberg: Iceberg A23a drift track in 2024

—T. SCAMBOS, C. SHUMAN, P. REID, A. MEIJERS, M. MEREDITH, AND J. LIESER

Movement of the trillion-ton iceberg A23a in 2024 illustrated several processes that have only recently been appreciated as key drivers of large iceberg drift. Foremost among these are the Taylor Column effects beneath the ice plate (see explanation below), which causes the iceberg's movement to respond to bathymetric features far below the base of the ice (Stern et al. 2019). Another is iceberg spin, related to ocean surface slope oscillations due to the tidal cycle and the variations in thickness across the ice plate (MacAyeal et al. 2008; Scambos et al. 2008).

Iceberg A23a calved in 1986 from the Filchner Ice Shelf ice front, as a large rift named the "Grand Chasm" by explorers in the 1950s finally separated completely, releasing three large icebergs spanning the Filchner front (Ferrigno and Gould 1987), from west to east: A22, A23a, and A24. The much smaller A25 south of the three was also released. Originally, A23a was nearly 4000 km^2 and ~400 m thick. It drifted about 200 km northward and ran aground (Swithinbank et al. 1988; Griggs and Bamber 2011), and for the next 34 years moved very little, before finally drifting free in June 2020 (Barbat et al. 2021). In 2023 it moved northward along the continental slope break to the east of the Antarctic Peninsula, pushed along by the Weddell Gyre.

As 2024 began, A23a was northeast of the tip of the Antarctic Peninsula, about 150 km east of Elephant Island. Drift progressed to the east and northeast, with the iceberg also rotating about once every 25 days, although there were long periods of more rapid eastward transit where the iceberg moved laterally without rotating (NASA Worldview MODIS data, https://worldview.earthdata.nasa.gov).

Around 1 April 2024, A23a entered an area of trapped counterclockwise ocean flow centered over Pirie Bank, north of the South Orkney Islands (Fig. SB6.1). This trapped vortex is characterized as a Taylor Column, a rotating cylinder of water that, under the right flow conditions, can be created above a topographic obstacle in a rotating fluid (Taylor 1922). Such columns are widely known in fluid dynamics experiments and have been observed in atmospheric and oceanic environments above mountains and seamounts, respectively. They are believed to be widespread across the more topographically rugged regions of the Southern Ocean, for example at Maud Rise in the Weddell Sea, but also across various locations including the seamounts that comprise the South Scotia Ridge, one of which is Pirie Bank (Meredith et al. 2015). By early June, A23a had shifted about 75 km to the northwest and began a new pattern of oscillations for the next four months, likely reflecting the impact of time-varying incident ocean flow on the complex shape of the bathymetry.

Still another form of topographic control on iceberg drift can be caused by the keel depth of the iceberg itself in areas of flatter underlying oceanographic terrain. Recent studies have pointed out the strong relationship between sections of iceberg drift tracks and deep bathymetric topography, with the moving iceberg steered in a way that avoids higher ridges or slopes (i.e., conserves potential vorticity in the column of water beneath the iceberg; Neuhaus and MacAyeal 2012; Scambos et al. 2024). Movement of A23a in mid-2023 along the eastern edge of the Antarctic Peninsula's continental slope and around Powell Basin in the northern Weddell Sea was likely guided by this process, as many other icebergs have been (Li et al. 2017).

A further process controlling iceberg flow on a daily to monthly scale is ocean tides. In the open ocean, tides are manifested as a cyclical change in ocean surface slope, typically in the range of a few parts in 10^{-4}. Like a surfboard, the iceberg slides downward on the ocean slope. The net effect of the daily tidal cycle is a circular iceberg movement that varies in amplitude with the bi-weekly tidal cycle, which is observable in the drift tracks of icebergs (Fig. SB6.2) with daily Global Navigation

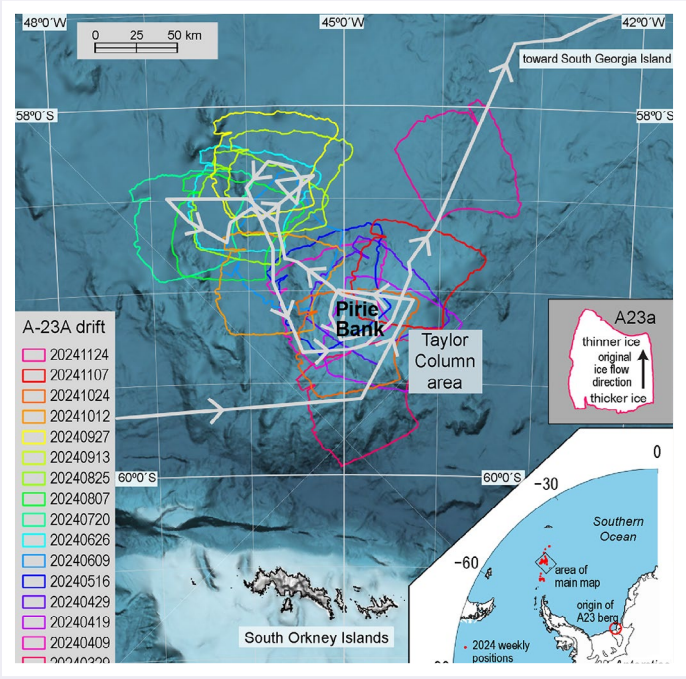

Fig. SB6.1. Bathymetric map of the region near Pirie Bank showing outlines of Iceberg A23a for several dates in 2024. Drift track with weekly positions of A23a shown as a gray line, with arrows showing drift direction. Lower right inset shows weekly positions of A23a for all of 2024 and original calving location of A23a on a regional map of Antarctica and the Southern Ocean; above that is an inset showing A23a outline with original orientation relative to ice flow on the Filchner Ice Shelf.

Satellite System (GNSS) data (MacAyeal et al. 2008; Scambos et al. 2008; Martin et al. 2010). Moreover, as part of this effect, the iceberg can be rotated based on the varying thickness of the ice across it, with the thicker (and therefore heavier) side tending to lead a bit more in the downslope direction. However, the response of large icebergs, like A23a, is generally too slow relative to the pace of tidally-driven ocean slope aspect change to execute daily rotations due to tides. Ocean current gradients and non-tidal sea surface slope variations further affect rotation and drift; thus, the observed rotation is complex and non-steady, particularly in the filamented and eddy-rich Antarctic Circumpolar Current.

Following the extended interaction with the Taylor Column above Pirie Bank, A23a drifted towards South Georgia in early 2025, threatening to run aground on its shoals and potentially disrupt the abundant ecosystems there as A38 did when it grounded there in 2004. Later in its evolution, A23a will succumb to basal thinning, flexure by long-period ocean waves, and meltwater-driven hydrofracture, leading to rapid calving and disintegration.

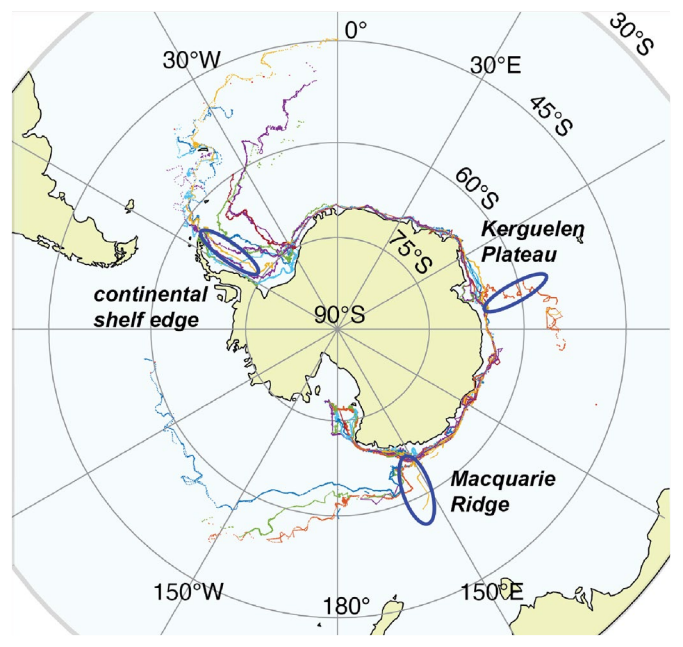

Fig. SB6.2. Map of the drift tracks of all major calved pieces of Icebergs B-15 and C-19—two of the largest icebergs in the historical record that calved from the Ross Ice Shelf front in 2000 and 2002, respectively—serving as an illustration of typical drift paths of Antarctic tabular icebergs. Drift track orientations are affected by deep bathymetry throughout the Southern Ocean; three bathymetric features where icebergs are guided out of westward circumpolar drift are labeled. Drift track data from Budge and Long (2018).

g. Southern Ocean

—S. J. Thomalla, A. M. Hancock, R. L. Beadling, A. Josey, J. Milward, A. Mohamed, L. P. Pezzi, M. du Plessis, T. J. Ryan-Keogh, C. Schulz, J-R. Shi, and E. Souza

The Southern Ocean (SO) plays a disproportionately large role in regulating Earth's climate through the uptake of heat and carbon dioxide (CO_2; Frölicher et al. 2015). The SO drives global ocean circulation and supplies oxygen to the deep ocean and nutrients worldwide (Oschlies et al. 2018; Henley et al. 2020). The SO is undergoing rapid change culminating in substantial warming and record-low sea ice extent, with cascading impacts on ocean biogeochemistry (Beadling et al. 2022; Pezzi et al. 2023; Thomalla et al. 2024). Here, the state of the SO in 2024 is assessed, with focus on a suite of physical and biogeochemical properties that influence SO ventilation and its capacity to take up heat and carbon. In 2024, the SO experienced substantial warming, continuing the warming trend of recent years (Cai et al. 2023) with ocean heat content (OHC) reaching its highest level to date. In some sectors, higher-than-usual salinities and shallower mixed layers were associated with a shift toward a negative Southern Annular Mode (SAM) from August to December (section 6b). Ocean biogeochemistry responded with elevated summer chlorophyll and lower surface oxygen in the Atlantic and eastern Pacific. These findings underscore the consequences of evolving atmosphere–ocean dynamics, reinforcing the SO's critical role in regulating climate.

1. SEA SURFACE TEMPERATURE, SALINITY, AND MIXED-LAYER PROPERTIES

Anomalies for 2024 (relative to a 1991–2020 climatology) were calculated for sea surface temperature (SST) from the NOAA monthly Optimum Interpolation product (Reynolds et al. 2002). Anomalies were calculated for sea surface salinity (SSS) and mixed-layer depth (MLD; according to de Boyer Montegut et al. 2004) from the Argo dataset (Roemmich and Gilson 2009), relative to a 2004–20 climatology. Abnormally warm surface waters prevailed across most of the SO, with positive SST anomalies (+0.4°C to +1.5°C; Fig. 6.14a) persisting throughout the year, following the warming tendency of previous years (Beadling et al. 2022; Pezzi et al. 2023; Thomalla et al. 2024). This was most notable in the western Pacific from February to July (Fig. 6.14e). The exceptions were the eastern Pacific, along the west coast of South America, and Drake Passage, where negative anomalies (−0.3°C to −0.6°C) reveal surface cooling in February and March (Fig. 6.14e). Positive anomalies in SSS (up to 0.20 PSU) dominate large parts of the SO (Fig. 6.14b), especially in spring, with the most extreme (~0.12 PSU) occurring in the Atlantic sector (Fig. 6.14f). These positive SSS anomalies typically occur north of the Subantarctic Front (SAF) and along the southern edge of subtropical gyres (STGs), possibly indicative of a strengthened gyre and enhanced salt import into the SO. A spin up of the STG was expected for the latter half of the year coinciding with the predominantly negative SAM phases. Weak negative anomalies in SSS were observed in summer/autumn (January–May), predominantly due to anomalies in the western Pacific (Fig. 6.14f) north of the SAF (Fig. 6.14b). The pattern of MLD anomalies in the SO is starkly different from recent years (2021–23), where persistent positive anomalies reflected deeper MLDs in the East Pacific (Beadling et al. 2022; Pezzi et al. 2023; Thomalla et al. 2024). In 2024, both Pacific sectors instead show significant shoaling of MLDs with negative anomalies north of the SAF and in the Indian sector south of Australia (Fig. 6.14c). For most sectors the onset of negative MLD anomalies occurred in May/June and peaked in August/September. This seasonal pattern aligns with the timing of positive SSS anomalies when the SAM shifted into a persistent negative phase favoring shallower MLDs when the westerlies shift equatorward into subtropical regions of anomalously positive SSS.

2. AIR–SEA HEAT FLUX

The 2024 net air–sea heat flux anomaly was determined using monthly mean ERA5 reanalysis (Hersbach et al. 2020) relative to the 1991–2020 climatology. Higher-than-average air–sea fluxes occurred across most of the subpolar SO, depicting anomalous ocean heat gain. Negative heat fluxes in the lower latitudes of the Atlantic (Fig. 6.14d) suggest anomalous ocean cooling in winter (Fig. 6.14h). North of the SAF, the imprint of ocean mesoscale variability on the air–sea flux is evident in alternating positive and negative anomalies, particularly in the Algulhas Retroflection region of South Africa extending into the Indian sector along ~60°S (Fig. 6.14d).

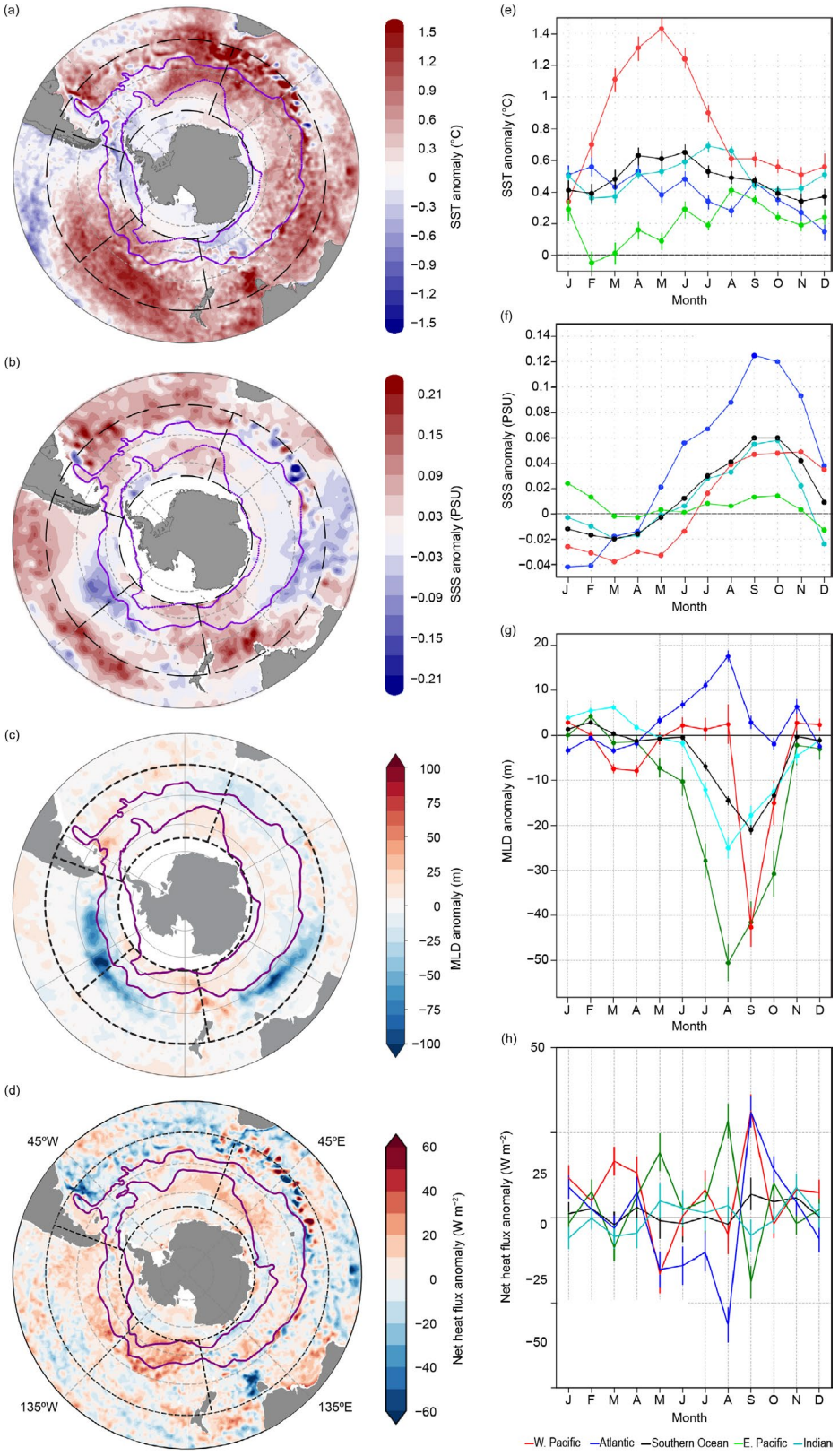

Fig. 6.14. Annual average (Jan–Dec 2024) anomalies of Southern Ocean (a) sea surface temperature (SST; °C; relative to 1991–2020 climatology), (b) sea surface salinity (SSS; PSU), (c) mixed-layer depth (MLD; m; relative to 2004–20 climatology), and (d) net heat flux (W m^{-2}; relative to 1991–2020 climatology). Overlaid are the positions of the Subantarctic and Southern Boundary Antarctic Circumpolar fronts (purple lines) as defined by Orsi et al. (1995). Four distinct sectors between 40°S and 65°S are delineated by black dashed contours corresponding to the Atlantic (70°W–20°E), Indian (20°E–170°E), western Pacific (170°W–120°W), and eastern Pacific (120°W–70°W). The 2024 seasonal cycle of anomalies in (e) SST (°C), (f) SSS (PSU), (g) MLD (m), and (h) net heat flux (W m^{-2}) are separated according to the four sectors defined above. Error bars in (e), (g), and (h) represent the standard error of the climatological mean (i.e., std. dev. divided by √N, where N is the number of years in the climatology).

Additional cooling in winter is also to be expected at high latitudes close to the Antarctic, as ongoing sea ice declines have recently been shown to substantially increase winter ocean heat loss to the atmosphere (Josey et al. 2024). Averaged across the SO, the mean net air–sea heat flux was 1.5 W m^{-2} higher than the climatology, albeit with considerable variability within the different sectors. In particular, the east Pacific and Atlantic sectors displayed large monthly mean heat flux changes in spring that exceed 30 W m^{-2} and 50 W m^{-2}, respectively (Figure 6.14h). The SO heat flux asymmetry index (Josey et al. 2023), which measures the difference in Atlantic–Indian and Pacific sector surface heat exchange, was –0.96 in 2024, which is a slight weakening of the degree of asymmetry relative to the 2023 value of –1.48.

3. UPPER-OCEAN HEAT CONTENT

The 0 m–2000 m upper OHC was retrieved from monthly gridded Argo temperature data (Roemmich and Gilson 2009) with 2024 anomalies determined relative to the 2004–20 climatology. The upper ocean gained heat in 2024 (Fig 6.15a) with positive OHC anomalies mainly north of the SAF. The upper ocean cooling observed in the eastern Pacific in 2023 (Thomalla et al. 2024), became neutral in 2024, with most of the SO exhibiting positive OHC anomalies (increased by 4.1 ZJ compared to 2023). Based on the records from the past two decades, the time series of the OHC anomaly shows long-term warming since 2005, reaching its highest level to date in 2024 (Fig. 6.15b).

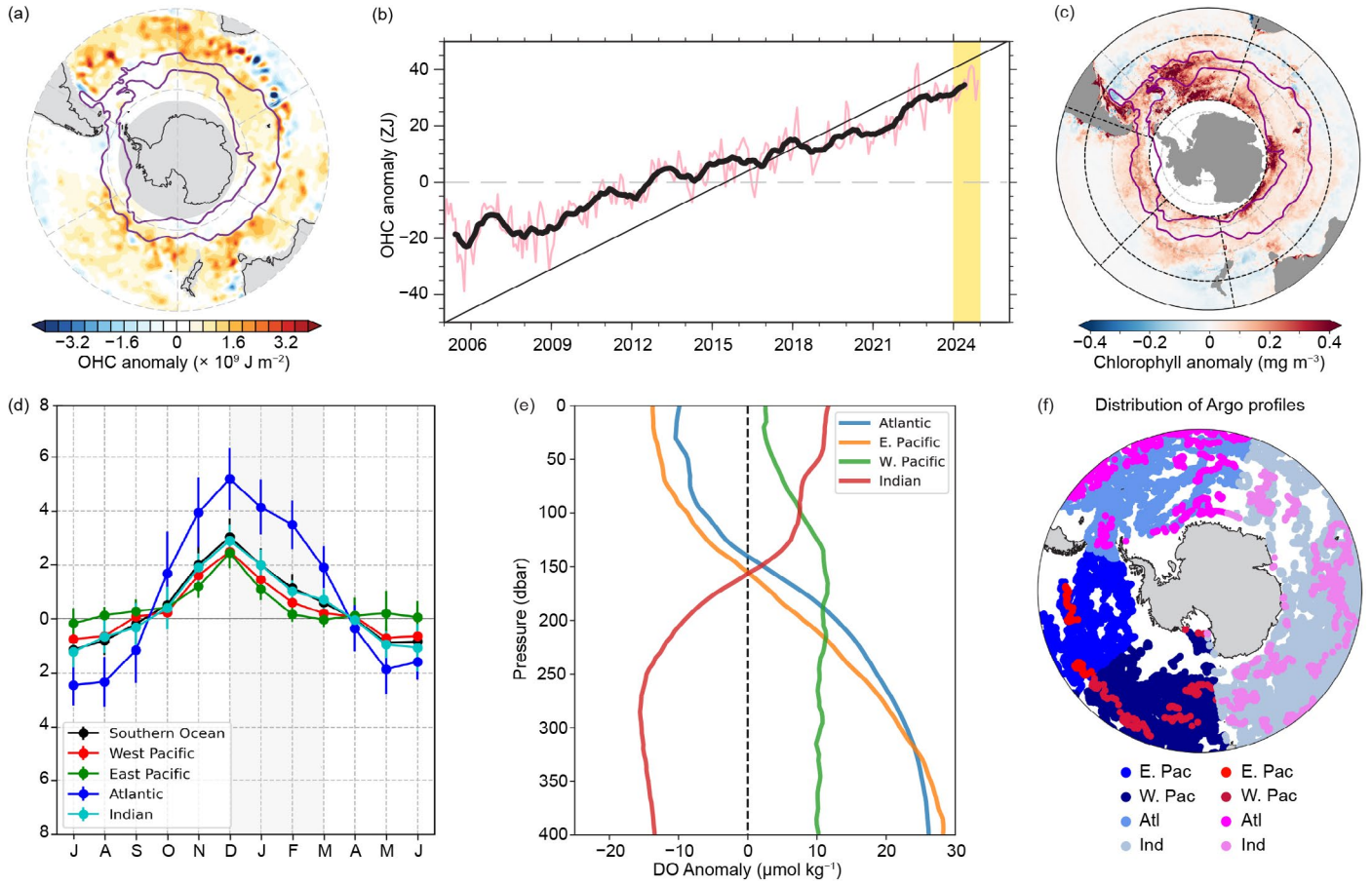

Fig. 6.15. (a) 2024 annual average ocean heat content (OHC; × 10^9 J m^{-2}) anomalies. (b) Time series of monthly average 0 m–2000 m OHC anomaly (ZJ or 10^{21} J) relative to 2004–20 Argo climatology within 40°S–65°S (red line) with 12-month running mean on top (black line) and 2024 highlighted (yellow shading). (c) Annual average (Jul 2023–Jun 2024) anomalies of eight-day, 4-km chlorophyll (mg m^{-3}) relative to 1999–2020 climatology and (d) the 2024 seasonal cycle of anomalies for the Atlantic (70°W–20°E), Indian (20°E–170°E), western Pacific (170°W–120°W), and eastern Pacific (120°W–70°W) between 40°S and 65°S. Error bars represent the standard error of the climatological mean (i.e., std. dev. divided by √N, where N is the number of years in the climatology). Overlaid on (a) and (c) are the Subantarctic and Southern Boundary Antarctic Circumpolar fronts (purple lines) as defined by Orsi et al. (1995). (e) Dissolved oxygen (DO) anomalies (μmol kg⁻¹) with pressure (dbar) for Jul 2023–Jun 2024 relative to the 2004–20 Argo climatology. (f) Distribution of Argo profiles from 2004–20 for the different ocean sectors (blues) relative to the distribution of profiles for the 2023/24 period (pinks and red).

4. OCEAN BIOGEOCHEMISTRY

Chlorophyll data from the eight-day European Space Agency Ocean Colour Climate Change Initiative (OC-CCI) product (v6.0; Sathyendranath et al. 2019) were processed as per Thomalla et al. (2023) with 2024 anomalies computed relative to the 1999–2020 climatology. Positive anomalies dominated the SO south of the SAF (Fig. 6.15c) in austral summer (Fig. 6.15d), most notably in the Atlantic (Weddell Gyre and east coast of South America) and Indian (south of 60°S) sectors, where higher-than-usual chlorophyll concentrations occurred (anomalies up to 0.4 mg m^{-3}). Weaker negative anomalies (<0.2 mg m^{-3}) were more persistent north of the SAF (Fig. 6.15c) in autumn (Fig. 6.15d). Anomalies in dissolved oxygen (DO) for 2024 (relative to 2004–20 climatology) were derived per ocean basin from BGC-Argo (Wong et al. 2020). The Indian sector showed positive DO anomalies from the surface to ~150 m, consistent with 2023 (Fig. 6.15e). In the Atlantic, where positive anomalies in chlorophyll were largest, DO anomalies were instead negative near the surface and positive below 150 m (Fig. 6.15e), indicating that the large positive SST anomalies are more likely driving the surface signal in DO. In the eastern Pacific, DO profiles were biased toward lower latitudes (Fig. 6.15f), where muted chlorophyll anomalies make SST anomalies the likely driver of negative DO anomalies near the surface. In the western Pacific, low positive anomalies persist from the surface to 400 m, likely influenced by positive chlorophyll anomalies or by profiles near the continent (Fig. 6.15f).

h. 2024 Antarctic ozone hole

—L. R. Lait, P. A. Newman, N. A. Kramarova, B. Johnson, M. L. Santee, I. Petropavlovskikh, L. Coy, and J. De Laat

The 2024 Antarctic ozone hole ranked in the lower third in severity (26th largest area over 32 years of observations) during the period of full ozone hole development (1992–present). The 2024 ozone hole had an average of 19.6 million km^2 average area (averaged 7 September–13 October). In 2024 the daily minimum average over 21 September–16 October was 121 Dobson units (DU; 23rd highest), 5 DU higher than the average of the 1992–2023 minimum averages. The 2024 ozone hole appeared later than average and reached 22.4 million km^2 in area on 28 September, in contrast to the record 29.9 million km^2 on 9 September 2000.

The 2024 Antarctic polar vortex evolution was relatively normal in early winter. May 2024 water vapor was higher than average inside the developing vortex because of the January 2022 Hunga volcanic eruption (Fig. 6.16b, purple line). As in 2023 (Kramarova et al. 2024; Santee et al. 2024), in 2024 water vapor abundances started high (Fig. 6.16b), but dehydration led to values only slightly above average by August. Polar cap (60°S–90°S) temperature in the stratosphere (50 hPa)

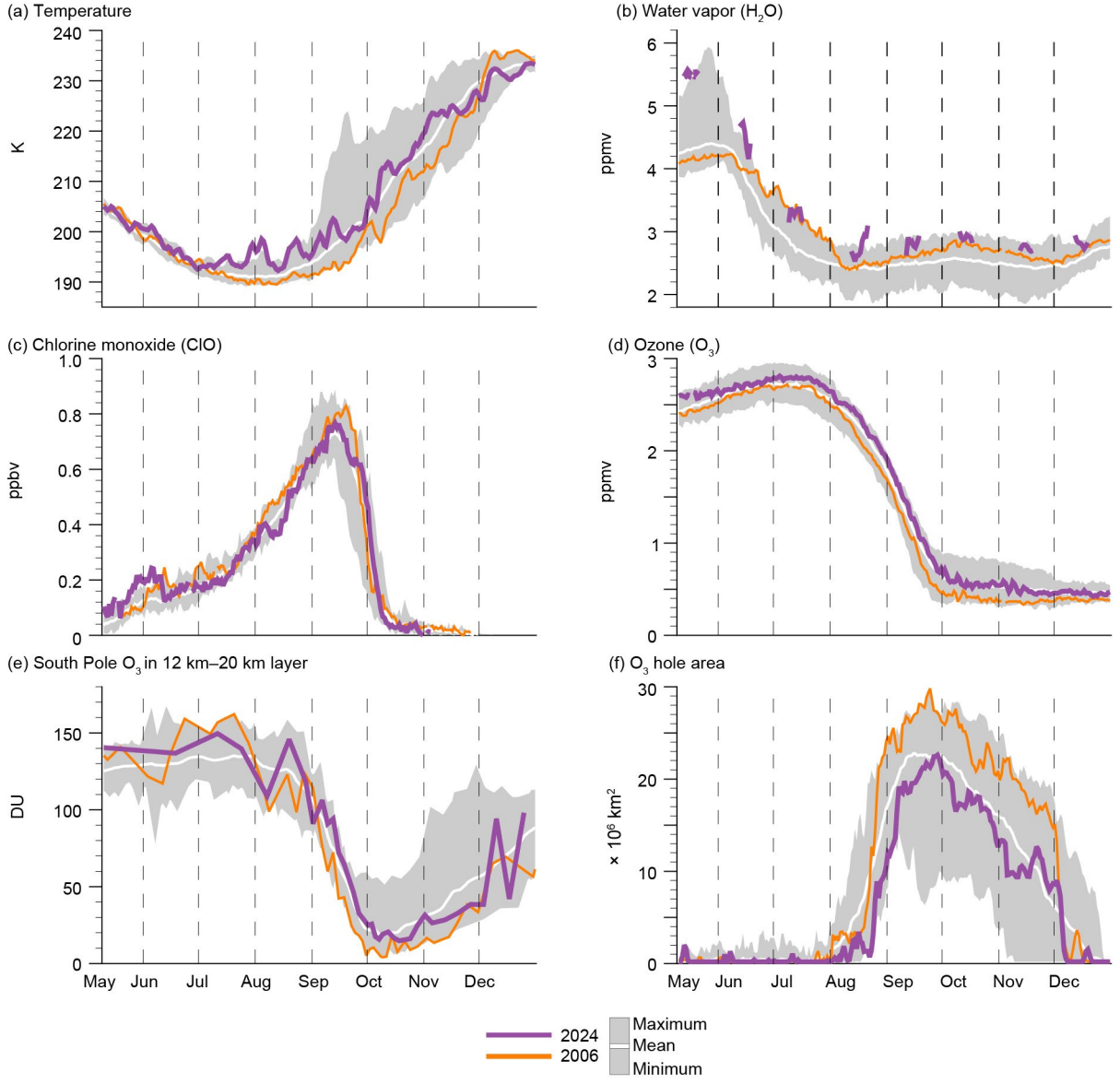

Fig. 6.16. Antarctic (a) polar cap temperature (K) at 50 hPa (~20 km or 60 hPa, averaged 60°S–90°S) from MERRA-2. Aura Microwave Limb Sounder (MLS; updated from Manney et al. 2011) 440-K potential temperature surface (b) water (H_2O; ppmv), (c) chlorine monoxide (ClO; ppbv), and (d) ozone (O_3; ppmv). (e) Lower-stratospheric ozone columns (12 km–20 km; DU) based on sonde measurements at South Pole. (f) Ozone Monitoring Instrument (OMI)/Ozone Mapping and Profiler Suite (OMPS) Antarctic ozone hole area (× 10^6 km^2; area with ozone total column less than 220 DU). Gray shading shows daily Antarctic value ranges for 2005–23 (for [d], the data cover 2006–23). The white lines indicate the 2005–23 long-term means.

was above average during late July and August (Fig. 6.16a). This above-average temperature slightly limited dehydration, resulting in above-average H_2O in June–December. There were no 2024 polar stratospheric cloud (PSC) measurements because the NASA Cloud–Aerosol Lidar and Infrared Pathfinder Satellite Observations (CALIPSO) lidar instrument ceased operation in June 2023.

Stratospheric wave driving from the troposphere (not shown) was anomalously large in mid-winter, warming the vortex and reducing the polar night jet's strength. Stratospheric wave driving is proportional to the eddy heat flux, which was relatively normal until mid-May. An extremely strong wavenumber-2 Rossby wave developed during mid-May to mid-August, increasing the heat flux (not shown). This wavenumber-2 pattern warmed the Antarctic stratosphere from late July to early August 2024 (section 6b). The wave-2 amplitude hit a global daily record high of 1511 geopotential meters (gpm) on 5 August at 10 hPa and exceeded 900 gpm from 25 July to 10 August, resulting in a 5.5 K temperature increase between 24 July and 4 August (Fig. 6.16a). The 4 August temperature was 6.7 K above the 1980–2023 average. Additionally, this wave transported ozone into the polar cap. Polar cap (63°S–90°S) ozone increased 24 DU between 25 July and 5 August 2024, a period when total ozone column typically declines by ~10 DU.

The wave-2 warming event was the proximate cause of the delayed 2024 ozone hole development. The opening of the ozone hole is defined as the date when the area exceeds 7 million km^2. Based on this threshold, the 2024 ozone hole started on 25 August, compared to an average of 18 August between 1992 and the present day. The 2024 delayed formation is consistent with South Pole ozonesonde data (Fig. 6.16e) and vortex-averaged ozone from the Microwave Limb Sounder (MLS; Fig. 6.16d), with both showing higher-than-average mid-winter ozone concentrations.

Ozone depletion rates in August–September 2024 were comparable to previous years, with 2006 being the most severe ozone hole in area and depth. Ozone loss rates were slightly smaller in 2024 than 2006, but both years averaged 40 ppb–50 ppb-per-day losses in early September. PSCs provide surface areas for heterogeneous reactions that convert reservoir chlorine species into active forms (e.g., chlorine monoxide, ClO; Fig. 6.16c). ClO catalytically destroys ozone. While PSC observations were not available in 2024, record-high vortex ClO abundances in May–June (>200 parts per trillion [ppt]) suggest greater early activation and likely greater PSC formation than average (as would be expected because of the Hunga injection of water into the stratosphere). In 2024, chlorine activation generally followed the typical seasonal pattern after early winter.

The ozone hole severity peaked in the late-September to early-October period. The largest single-day area was 22.4 million km^2 (28 September; Fig. 6.16f), the minimum polar cap ozone value was 107 DU on 5 October, the mass deficit was 28.2 million metric tons of ozone (28 September), and the polar cap (63°S–90°S) average ozone was 210 DU (27 September). The South Pole ozone sonde 12 km–20 km column bottomed out in early October and had an absolute 14.8-DU minimum (18 October; Fig. 6.16e).

The ozone hole had near-average September values. Most Antarctic ozone depletion occurs in the August and September period (Figs. 6.16d–f), making September the key period for evaluating the chemical depletion severity. Figure 6.17a displays September average hole area versus year, separated into colder years (lower third, blue triangles), average years (middle third, black dots), and warmer years (upper third, red squares). Year-to-year temperature variability modulates hole severity, with colder (warmer) years leading to greater (lesser) ozone depletion and less (more) ozone advection into the Antarctic polar region (Fig. 6.17b). The 2024 temperature (purple triangle) was near average, leading to a near-zero-hole anomaly. Because of the decreased levels of chlorine and bromine in the Antarctic polar vortex, the 2024 hole was not as deep or extensive as those observed in the early 2000s.

The 2024 ozone hole broke up on 21 December (Fig. 6.17c), two weeks after the 7 December average calculated from the 1992–2024 period (dashed line). The breakup is calculated as the final date with observed total ozone values less than 220 DU in the Antarctic region (Fig. 6.17f). An increasing trend from November to December hole breakup dates is seen from 1979 to 1991 (Fig. 6.17c). As levels of chlorine and bromine decline, the hole breakup should fall back into November. However, there is no apparent breakup trend in the 2000–24 period (Fig. 6.17c), in

remarkable contrast to the recovery in the September hole area (Fig. 6.17a). The November hole area is linearly related to the November 50-hPa polar cap temperature (Fig. 6.17d). Colder- (warmer-) than-average temperatures lead to a larger (smaller) November hole remnant, and therefore a later (earlier) breakup date. The November 2024 temperature was near average, somewhat consistent with the 21 December 2024 breakup. The last five years (2020–24) have seen late breakups, in contrast to the 2013–19 period. These late breakups are not caused by chemically driven loss but rather suggest variability or trends of the stratospheric dynamics in the last five years.

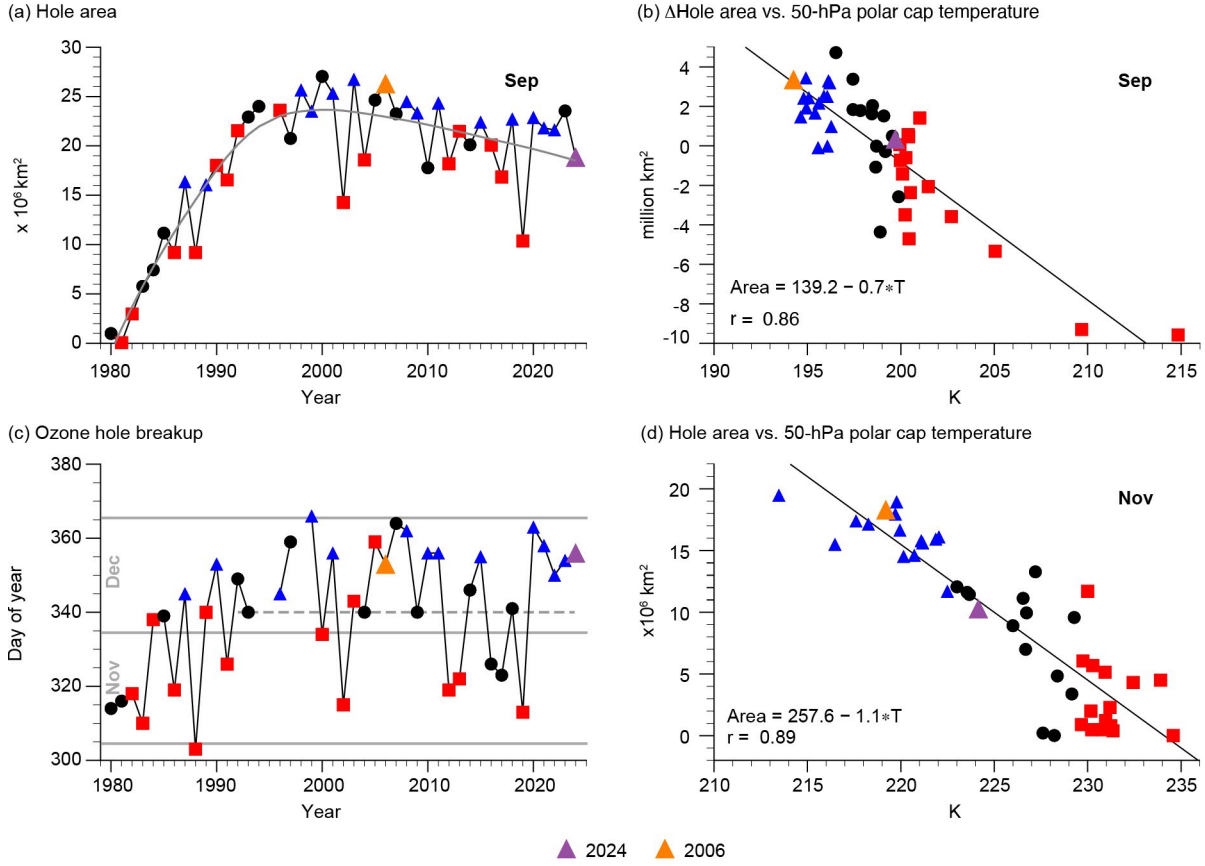

Fig. 6.17. (a) Annual Sep average Antarctic ozone hole area (× 10^6 km^2). (b) Sep ozone hole area anomalies (see text) vs. MERRA-2 Sep 50-hPa temperatures (K) averaged over the polar cap (60°S–90°S). (c) Ozone hole break-up dates, where the horizontal dashed line is the 1992–2024 average. (d) Nov ozone hole areas vs. MERRA-2 Nov 50-hPa temperatures. In (a), the gray curve shows a quadratic fit of effective equivalent stratospheric chlorine with a 5.2-year mean age of air (Newman et al. 2007) to the Sep hole areas. Years with temperatures in the lowest (highest) third are shown as blue triangles (red squares). The years 2006 and 2024 are specifically highlighted in orange and purple, respectively. Ozone data for 1979–92 are from Total Ozone Mapping Spectrometer (TOMS) Nimbus-7; data for 1993/94 are from TOMS Meteor-3; data for 1996–2004 are from TOMS Earth Probe; data for 2005–15 are from Aura Ozone Monitoring Instrument (OMI); and data for 2015–24 are from Suomi National Polar-orbiting Partnership (SNPP) Ozone Mapping and Profiler Suite (OMPS). There are no 1995 satellite mapper total ozone observations.

Acknowledgments

- K. R. Clem and M. N. Raphael would like to acknowledge and thank Samuel Batzli, University of Wisconsin-Madison, for kindly producing the map shown in Fig. 6.1.
- Work at the California Institute of Technology's Jet Propulsion Laboratory was done under contract with NASA. Support was also provided by the NASA Earth Science Division's Modeling and Analysis Program and the Upper Atmospheric Research Program. We are indebted to the many NOAA Corps Officers and Global Monitoring Laboratory technical personnel, who spend the winters at South Pole Station to obtain the ongoing balloon and ground-based data sets. We also acknowledge the logistics support in Antarctica provided by the National Science Foundation (NSF) Office of Polar Programs.

- P. Reid and J. Lieser were supported through Australia's Bureau of Meteorology, and R. Massom by the Australian Antarctic Division. The work of P. Reid and R. Massom also contributes to the Australian Government's Australian Antarctic Partnership Program (AAPP). For R. Massom, this work was also supported by the Australian Research Council Special Research Initiative of the Australian Centre for Excellence in Antarctic Science (Project Number SR200100008).
- S. Stammerjohn was supported under NSF PLR–1552226; she also thanks the Institute of Arctic and Alpine Research and the National Snow and Ice Data Center, both at the University of Colorado Boulder, for institutional and data support.
- The Southern Ocean Observing System is a joint international initiative of the Scientific Committee on Antarctic Research (SCAR) and the Scientific Committee on Oceanic Research (SCOR).
- L. P. Pezzi acknowledges support from the Brazilian Antarctic Program's (PROANTAR) Antarctic Modeling and Observation System (ATMOS 2) project under the National Council for Scientific and Technological Development (CNPq)/PROANTAR award 440848/2023-7 and PQ 303981/2023-7.
- R. L. Beadling and J. Milward were supported under the NSF Division of Polar Programs Grant NSF2319828.
- S. Thomalla and T. J. Ryan-Keogh were supported through the Council for Scientific and Industrial Research's (CSIR) Southern Ocean Carbon-Climate Observatory (SOCCO) Programme (http://socco.org.za/) funded by the Department of Science and Innovation (DSI/CON C3184/2023), the CSIR's Parliamentary Grant (0000005278), and the National Research Foundation (SANAP23042496681; MCR210429598142).
- K. R. Clem acknowledges support from the Royal Society of New Zealand Marsden Fund grant MFP-VUW2010.

Appendix 1: Acronyms

AIS	Antarctic Ice Sheet
AMRDC	Antarctic Meteorological Research and Data Center
AR	atmospheric river
AWS	automatic weather station
CALIPSO	Cloud–Aerosol Lidar and Infrared Pathfinder Satellite Observations
ClO	chlorine monoxide
CRI	Coastal Resolution Improvement
DMSP	Defense Meteorological Satellite Program
DO	dissolved oxygen
DU	Dobson unit
EPE	extreme precipitation event
ESA	European Space Agency
GNSS	Global Navigation Satellite System
GRACE	Gravity Recovery and Climate Experiment
GRACE-FO	Gravity Recovery and Climate Experiment Follow-On
IMBIE	Ice Mass Balance Intercomparison Exercise
MAR	Model for Surface Mass Balance of the Arctic Ice Sheets
MLD	mixed-layer depth
MLS	Microwave Limb Sounder
NRTSI	Near-Real-Time Defense Meteorological Satellite Program Special Sensor Microwave Imager Sounder Daily Polar Gridded Sea Ice Concentrations
NSIDC	National Snow and Ice Data Center
OC-CCI	Ocean Colour Climate Change Initiative
OHC	ocean heat content
OMI	Ozone Monitoring Instrument
OMPS	Ozone Mapping and Profiler Suite
P–E	total precipitation minus evaporation and sublimation
PSC	polar stratospheric cloud
SAF	Subantarctic Front
SAM	Southern Annular Mode
SAR	synthetic aperture radar
SIA	sea ice area
SIE	sea ice extent
SMB	surface mass balance
SMMR	Scanning Multichannel Microwave Radiometer
SNPP	Suomi National Polar-orbiting Partnership
SO	Southern Ocean
SSM/I	Special Sensor Microwave Imager
SSMIS	Special Sensor Microwave Imager Sounder
SSS	sea surface salinity
SST	sea surface temperature
STG	subtropical gyre
TOMS	Total Ozone Mapping Spectrometer
vIVT	vector-invariant water transport
WAIS	West Antarctic Ice Sheet

Appendix 2: Datasets and sources

Section 6b Atmospheric circulation and surface observations

Sub-section	General Variable or Phenomenon	Specific Dataset or Variable	Source
6b	Geopotential Height	ERA5	https://www.ecmwf.int/en/forecasts/dataset/ecmwf-reanalysis-v5
6b	Modes of Variability	Marshall Southern Annular Mode Index	http://www.nerc-bas.ac.uk/icd/gjma/sam.html
6b	Pressure, Sea Level or Near-Surface	ERA5	https://www.ecmwf.int/en/forecasts/dataset/ecmwf-reanalysis-v5
6b	Pressure, Sea Level or Near-Surface	University of Wisconsin-Madison Automated Weather Stations—Antarctic Meteorological Research and Data Center	https://amrdcdata.ssec.wisc.edu
6b	Pressure, Sea Level or Near-Surface	Staffed Weather Station Data	https://legacy.bas.ac.uk/met/READER/
6b	Temperature, [Near] Surface	ERA5	https://www.ecmwf.int/en/forecasts/dataset/ecmwf-reanalysis-v5
6b	Temperature, [Near] Surface	University of Wisconsin-Madison Automated Weather Stations—Antarctic Meteorological Research and Data Center	https://amrdcdata.ssec.wisc.edu
6b	Temperature, [Near] Surface	Staffed Weather Station Data	https://legacy.bas.ac.uk/met/READER/
6b	Temperature, Upper-Atmosphere	ERA5	https://www.ecmwf.int/en/forecasts/dataset/ecmwf-reanalysis-v5
6b	Wind, Upper-Atmosphere	ERA5	https://www.ecmwf.int/en/forecasts/dataset/ecmwf-reanalysis-v5

Section 6c Ice sheet surface mass balance

Sub-section	General Variable or Phenomenon	Specific Dataset or Variable	Source
6c	Ice Sheet Surface Mass Balance	Polar-Oriented Regional Climate Model (Model for Surface Mass Balance of the Arctic Ice Sheets [MAR])	https://arcticdata.io/catalog/view/doi%3A10.18739%2FA28G8FJ7F
6c	Ice Sheet Surface Mass Balance	ERA5	https://www.ecmwf.int/en/forecasts/dataset/ecmwf-reanalysis-v5
6c	Ice Sheet Surface Mass Balance	MERRA-2	http://gmao.gsfc.nasa.gov/reanalysis/MERRA-2/

Section 6d Ice sheet melt extent and duration

Sub-section	General Variable or Phenomenon	Specific Dataset or Variable	Source
6d	Ice Sheet Surface Melt	Defense Meteorological Satellite Program (DMSP) Special Sensor Microwave Imager/Sounder (SSMIS)	https://nsidc.org/data/nsidc-0001/versions/6
6d	Sea Ice Extent/Area/ Concentration	Nimbus-7 Scanning Multichannel Microwave Radiometer (SMMR) Sea Ice Concentration	https://nsidc.org/data/nsidc-0007

Section 6e Ice sheet mass balance

Sub-section	General Variable or Phenomenon	Specific Dataset or Variable	Source
6e	Ice Sheet Surface Height	Advanced Topographic Laser Altimeter System (ATLAS) Ice, Cloud and Land Elevation Satellite-2 (ICESat-2)	https://nsidc.org/data/atl06/versions/5
6e	Ice Sheet Surface Height	ICESat-2	https://icesat-2.gsfc.nasa.gov/
6e	Ice Sheet Mass	Gravity Recovery and Climate Experiment (GRACE)/GRACE Follow-On (GRACE-FO)	https://podaac.jpl.nasa.gov/dataset/TELLUS_GRAC-GRFO_MASCON_CRI_GRID_RL06_V2

Section 6f Sea ice extent, concentration, and seasonality

Sub-section	General Variable or Phenomenon	Specific Dataset or Variable	Source
6f	Sea Ice Extent and Area	Near-Real-Time Defense Meteorological Satellite Program (DMSP) Special Sensor Microwave Imager/ Sounder (SSMIS) Daily Polar Gridded Sea Ice Concentrations, Version 1	https://arcticdata.io/catalog/view/doi:10.18739/A2B56D64V
6f	Sea Surface Temperature	NOAA OISSTv2.1	https://www.ncei.noaa.gov/products/optimum-interpolation-sst

Section 6g Southern Ocean

Sub-section	General Variable or Phenomenon	Specific Dataset or Variable	Source
6g1	Sea Surface Temperature	NOAA OISSTv2.1	https://www.ncei.noaa.gov/products/optimum-interpolation-sst

Sub-section	General Variable or Phenomenon	Specific Dataset or Variable	Source
6g1	Sea Surface Salinity	Argo Monthly Climatology	https://sio-argo.ucsd.edu/RG_Climatology.html
6g1	Mixed-Layer Depth	Argo Monthly Climatology	https://sio-argo.ucsd.edu/RG_Climatology.html
6g2	Surface Heat flux	ERA5	https://www.ecmwf.int/en/forecasts/dataset/ecmwf-reanalysis-v5
6g3	Ocean Heat Content	Argo Monthly Climatology	https://sio-argo.ucsd.edu/RG_Climatology.html
6g4	Dissolved Oxygen	Biogeochemical Argo (BGC-Argo)	https://biogeochemical-argo.org/
6g4	Ocean Chlorophyll	ESA Ocean Colour Climate Change Initiative (OC-CCI) product Version 6.0	https://www.oceancolour.org/

Section 6h 2024 Antarctic ozone hole

Sub-section	General Variable or Phenomenon	Specific Dataset or Variable	Source
6h	Cloud Volume	CALIPSO	http://www-calipso.larc.nasa.gov
6h	Temperature, [Near] Surface	MERRA-2	http://gmao.gsfc.nasa.gov/reanalysis/MERRA-2/
6h	Temperature, Upper-Atmosphere	MERRA-2	https://gmao.gsfc.nasa.gov/reanalysis/MERRA-2/
6h	Ozone, Total Column and Stratospheric	Aura Microwave Limb Sounder (MLS)	http://disc.sci.gsfc.nasa.gov/Aura/data-holdings/MLS/index.shtml
6h	Ozone, Total Column and Stratospheric	Ozone Mapping Instrument (OMI) Ozone Mapping & Profiler Suite (OMPS), Total Ozone Mapping Spectrum (TOMS), Earth Probe TOMS (EPTOMS)	https://ozoneaq.gsfc.nasa.gov/data/ozone/
6h	Ozone, Lower Stratosphere	Ozonesonde	https://gml.noaa.gov/dv/spo_oz/

Sidebar 6.1: How to train your iceberg: Iceberg A23a drift track in 2024

Sub-section	General Variable or Phenomenon	Specific Dataset or Variable	Source
SB6.1	Iceberg Drift Tracks	NASA Worldview Moderate Resolution Imaging Spectroradiometer (MODIS) data	https://worldview.earthdata.nasa.gov

Sub-section	General Variable or Phenomenon	Specific Dataset or Variable	Source
SB6.1	Iceberg Drift Tracks	Global Navigation Satellite System (GNSS) data	https://cddis.nasa.gov/Data_and_Derived_Products/GNSS/daily_gnss_o.html

References

Agosta, C., and Coauthors, 2019: Estimation of the Antarctic surface mass balance using the regional climate model MAR (1979–2015) and identification of dominant processes. *Cryosphere*, **13**, 281–296, https://doi.org/10.5194/tc-13-281-2019.

AMRDC, 2022: Automatic Weather Station quality-controlled observational data. AMRDC Data Repository, accessed 30 January 2025, https://doi.org/10.48567/1hn2-nw60.

Banwell, A. F., D. R. MacAyeal, and O. V. Sergienko, 2013: Breakup of the Larsen B Ice Shelf triggered by chain reaction drainage of supraglacial lakes. *Geophys. Res. Lett.*, **40**, 5872–5876, https://doi.org/10.1002/2013GL057694.

Barbat, M. M., T. Rackow, C. Wesche, H. H. Hellmer, and M. M. Mata, 2021: Automated iceberg tracking with a machine learning approach applied to SAR imagery: A Weddell sea case study. *ISPRS J. Photogramm. Remote Sens.*, **172**, 189–206, https://doi.org/10.1016/j.isprsjprs.2020.12.006.

Beadling, R. L., N. M. Freeman, G. A. MacGilchrist, M. Mazloff, J.-R. Shi, A. F. Thompson, and E. Wilson, 2022: Southern Ocean [in "State of the Climate in 2021"]. *Bull. Amer. Meteor. Soc.*, **103** (8), S329–S332, https://doi.org/10.1175/BAMS-D-22-0078.1.

Budge, J. S., and D. G. Long, 2018: A comprehensive database for Antarctic iceberg tracking using scatterometer data. *IEEE J. Sel. Top. Appl. Earth Obs. Remote Sens.*, **11**, 434–442, https://doi.org/10.1109/JSTARS.2017.2784186.

Cai, W., and Coauthors, 2023: Southern Ocean warming and its climatic impacts. *Sci. Bull.*, **68** (9), 946–960, https://doi.org/10.1016/j.scib.2023.03.049.

Cavalieri, D. J., C. L. Parkinson, P. Gloersen, and H. J. Zwally, 1996: Sea ice concentrations from Nimbus-7 SMMR and DMSP SSM/I-SSMIS passive microwave data, version 1. NASA National Snow and Ice Data Center Distributed Active Archive Center, accessed 15 February 2025, https://doi.org/10.5067/8GQ8LZQVL0VL.

Cheng, L., and Coauthors, 2022: Past and future ocean warming. *Nat. Rev. Earth Environ.*, **3**, 776–794, https://doi.org/10.1038/s43017-022-00345-1.

Clem, K. R., and Coauthors, 2022: Antarctica and the Southern Ocean [in "State of the Climate in 2021"]. *Bull. Amer. Meteor. Soc.*, **103** (8), S307–S340, https://doi.org/10.1175/BAMS-D-22-0078.1.

—— , and Coauthors, 2023: Antarctica and the Southern Ocean [in "State of the Climate in 2022"]. *Bull. Amer. Meteor. Soc.*, **104** (9), S322–S365, https://doi.org/10.1175/BAMS-D-23-0077.1.

—— , and Coauthors, 2024: Antarctica and the Southern Ocean [in "State of the Climate in 2023"]. *Bull. Amer. Meteor. Soc.*, **105** (8), S331–S370, https://doi.org/10.1175/BAMS-D-24-0099.1.

Comiso, J. C., 2017: Bootstrap sea ice concentrations from Nimbus-7 SMMR and DMSP SSM/I-SSMIS, version 3. NASA National Snow and Ice Data Center Distributed Active Archive Center, accessed 2 February 2024, https://doi.org/10.5067/7Q8HCCWS4I0R.

Davison, B. J., and Coauthors, 2023: Sea level rise from West Antarctic mass loss significantly modified by large snowfall anomalies. *Nat. Commun.*, **14**, 1479, https://doi.org/10.1038/s41467-023-36990-3.

de Boyer Montégut, C., G. Madec, A. S. Fischer, A. Lazar, and D. Ludicone, 2004: Mixed layer depth over the global ocean: An examination of profile data and a profile-based climatology. *J. Geophys. Res.*, **109**, C12003, https://doi.org/10.1029/2004JC002378.

Ferrigno, J. G., and W. G. Gould, 1987: Substantial changes in the coastline of Antarctica revealed by satellite imagery. *Polar Rec.*, **23**, 577–583, https://doi.org/10.1017/S003224740000807X.

Fraser, A. D., and Coauthors, 2023: Antarctic landfast sea ice: A review of its physics, biogeochemistry and ecology. *Rev. Geophys.*, **61**, e2022RG000770, https://doi.org/10.1029/2022RG000770.

Frölicher, T. L., J. L. Sarmiento, D. J. Paynter, J. P. Dunner, J. P. Krasting, and M. Winton, 2015: Dominance of the Southern Ocean in anthropogenic carbon and heat uptake in CMIP5 models. *J. Climate*, **28**, 862–886, https://doi.org/10.1175/JCLI-D-14-00117.1.

Gelaro, R., and Coauthors, 2017: The Modern-Era Retrospective Analysis for Research and Applications, version 2 (MERRA-2). *J. Climate*, **30**, 5419–5454, https://doi.org/10.1175/JCLI-D-16-0758.1.

Gerrish, L., L. Ireland, P. Fretwell, and P. Cooper, 2023: High resolution vector polygons of the Antarctic coastline, version 7.8. UK Polar Data Centre, Natural Environment Research Council, UK Research & Innovation, accessed 8 February 2024, https://doi.org/10.5285/C7FE759D-E042-479A-9ECF-274255B4F0A1.

Gloersen, P., 2006: Nimbus-7 SMMR polar gridded radiances and sea ice concentrations, version 1. Subset: 37 & 19 GHz, h-polarization, 25 km grid, October 1979–April 1987. NASA National Snow and Ice Data Center Distributed Active Archive Center, accessed 5 May 2020, https://doi.org/10.5067/QOZIVYV3V9JP.

Gossart, A., S. Helsen, J. T. M. Lenaerts, S. V. Broucke, N. P. M. Van Lipzig, and N. Souverijns, 2019: An evaluation of surface climatology in state-of-the-art reanalyses over the Antarctic ice sheet. *J. Climate*, **32**, 6899–6915, https://doi.org/10.1175/JCLI-D-19-0030.1.

Griggs, J. A., and J. L. Bamber, 2011: Antarctic ice-shelf thickness from satellite radar altimetry. *J. Glaciol.*, **57**, 485–498, https://doi.org/10.3189/002214311796905659.

Haid, V., D. Iovino, and S. Masina, 2017: Impacts of freshwater changes on Antarctic sea ice in an eddy-permitting sea-ice–ocean model. *Cryosphere*, **11**, 1387–1402, https://doi.org/10.5194/tc-11-1387-2017.

Hanna, E., and Coauthors, 2024: Short- and long-term variability of the Antarctic and Greenland ice sheets. *Nat. Rev. Earth Environ.*, **5**, 193–210, https://doi.org/10.1038/s43017-023-00509-7.

Henley, S. F., and Coauthors, 2020: Changing biogeochemistry of the Southern Ocean and its ecosystem implications. *Front. Mar. Sci.*, **7**, 581, https://doi.org/10.3389/fmars.2020.00581.

Hersbach, H., and Coauthors, 2020: The ERA5 global reanalysis. *Quart. J. Roy. Meteor. Soc.*, **146**, 1999–2049, https://doi.org/10.1002/qj.3803.

Hosking, J. S., A. Orr, T. J. Bracegirdle, and J. Turner, 2016: Future circulation changes off West Antarctica: Sensitivity of the Amundsen Sea Low to projected anthropogenic forcing. *Geophys. Res. Lett.*, **43**, 367–376, https://doi.org/10.1002/2015GL067143.

—— , —— , G. J. Marshall, J. Turner, and T. Phillips, 2013: The influence of the Amundsen–Bellingshausen Seas low on the climate of West Antarctica and its representation in coupled climate model Ssimulations. *J. Climate*, **26**, 6633–6648, https://doi.org/10.1175/JCLI-D-12-00813.1.

Huang, B., C. Liu, V. Banzon, E. Freeman, G. Graham, B. Hankins, T. Smith, and H.-M. Zhang, 2021: Improvements of the Daily Optimum Interpolation Sea Surface Temperature (DOISST) version 2.1. *J. Climate*, **34**, 2923–2939, https://doi.org/10.1175/JCLI-D-20-0166.1.

Josey, S. A., J. P. Grist, J. V. Mecking, B. I. Moat, and E. Schulz, 2023: A clearer view of Southern Ocean air-sea interaction using surface heat flux asymmetry. *Philos. Trans. Roy. Soc.*, **A381**, 20220067, https://doi.org/10.1098/rsta.2022.0067.

—— , A. J. S. Meijers, A. T. Blaker, J. P. Grist, J. Mecking, and H. C. Ayres, 2024: Record-low Antarctic sea ice in 2023 increased ocean heat loss and storms. *Nature*, **636**, 635–639, https://doi.org/10.1038/s41586-024-08368-y.

Kittel, C., and Coauthors, 2021: Diverging future surface mass balance between the Antarctic ice shelves and grounded ice sheet. *Cryosphere*, **15**, 1215–1236, https://doi.org/10.5194/tc-15-1215-2021.

Kolbe, M., R. Bintanja, E. C. van der Linden, and R. R. Cordero, 2025: Vertical structure and surface impact of atmospheric rivers reaching Antarctic sea ice and land. *Atmos. Res.*, **315**, 107841, https://doi.org/10.1016/j.atmosres.2024.107841.

Kramarova, N. A., and Coauthors, 2024: 2023 Antarctic ozone hole [in "State of the Climate in 2023"]. *Bull. Amer. Meteor. Soc.*, **105** (8), S358–S361, https://doi.org/10.1175/BAMS-D-24-0099.1.

Lenaerts, J. T. M., B. Medley, M. R. van den Broeke, and B. Wouters, 2019: Observing and modeling ice sheet surface mass balance. *Rev. Geophys.*, **57**, 376–420, https://doi.org/10.1029/2018RG000622.

Li, T., and Coauthors, 2017: The effect of seafloor topography in the Southern Ocean on tabular iceberg drifting and grounding. *Sci. China Earth Sci.*, **60**, 697–706, https://doi.org/10.1007/s11430-016-9014-5.

MacAyeal, D. R., M. H. Okal, J. E. Thom, K. M. Brunt, Y. J. Kim, and A. K. Bliss, 2008: Tabular iceberg collisions within the coastal regime. *J. Glaciol.*, **54**, 371–386, https://doi.org/10.3189/002214308784886180.

MacFerrin, M., T. Mote, H. Wang, L. Liu, L. Montgomery, and T. Scambos, 2021: Ice sheet seasonal melt extent and duration [in "State of the Climate in 2020"]. *Bull. Amer. Meteor. Soc.*, **102**, S331–S334, https://doi.org/10.1175/BAMS-D-21-0081.1.

—— , —— , A. Banwell, and T. Scambos, 2022: Ice sheet seasonal melt extent and duration [in "State of the Climate in 2021"]. *Bull. Amer. Meteor. Soc.*, **103** (8), S321–S323, https://doi.org/10.1175/2022BAMSStateoftheClimate.1.

—— , —— , —— , and —— , 2023: Ice sheet seasonal melt extent and duration [in "State of the Climate in 2022"]. *Bull. Amer. Meteor. Soc.*, **104** (9), S339–S341, https://doi.org/10.1175/BAMS-D-23-0077.1.

Maclennan, M. L., J. T. M. Lenaerts, C. Shields, and J. D. Wille, 2022: Contribution of atmospheric rivers to Antarctic precipitation. *Geophys. Res. Lett.*, **49**, e2022GL100585, https://doi.org/10.1029/2022GL100585.

Manney, G. L., and Coauthors, 2011: Jet characterization in the upper troposphere/lower stratosphere (UTLS): Applications to climatology and transport studies. *Atmos. Chem. Phys.*, **11**, 6115–6137, https://doi.org/10.5194/acp-11-6115-2011.

Marshall, G. J., 2003: Trends in the Southern Annular Mode from observations and reanalyses. *J. Climate*, **16**, 4134–4143, https://doi.org/10.1175/1520-0442(2003)016<4134:TITSAM>2.0.CO;2.

Martin, S., R. Drucker, R. Aster, F. Davey, E. Okal, T. Scambos, and D. MacAyeal, 2010: Kinematic and seismic analysis of giant tabular iceberg breakup at Cape Adare, Antarctica. *J. Geophys. Res.*, **115**, B06311, https://doi.org/10.1029/2009JB006700.

Maslanik, J., and J. Stroeve, 1999: Near-real-time DMSP SSM/I-SSMIS daily polar gridded sea ice concentrations (updated daily). National Snow and Ice Data Center, accessed 15 February 2025, https://nsidc.org/data/docs/daac/nsidc0081_ssmi_nrt_seaice.gd.html.

Massom, R. A., T. A. Scambos, L. G. Bennetts, P. Reid, V. A. Squire, and S. E. Stammerjohn, 2018: Antarctic ice shelf disintegration triggered by sea ice loss and ocean swell. *Nature*, **558**, 383–389, https://doi.org/10.1038/s41586-018-0212-1.

Medley, B., and E. R. Thomas, 2019: Increased snowfall over the Antarctic Ice Sheet mitigated twentieth-century sea-level rise. *Nat. Climate Change*, **9**, 34–39, https://doi.org/10.1038/s41558-018-0356-x.

Meier, W. N., H. Wilcox, M. A. Hardman, and J. S. Stewart, 2019: DMSP SSM/I-SSMIS daily polar gridded brightness temperatures, version 5. Subset: 37 & 19 GHz, h-polarization, 25 km grid, October 1987–April 2020. NASA National Snow and Ice Data Center Distributed Active Archive Center, accessed 11 February 2021, https://doi.org/10.5067/QU2UYQ6T0B3P.

Meredith, M. P., and M. A. Brandon, 2017: Oceanography and sea ice in the Southern Ocean. *Sea Ice*, D. Thomas, Ed., Wiley, 216–238.

—— , A. S. Meijers, A. C. Naveira Garabato, P. J. Brown, H. J. Venables, E. P. Abrahamsen, L. Jullion, and M. J. Messias, 2015: Circulation, retention, and mixing of waters within the Weddell-Scotia Confluence, Southern Ocean: The role of stratified Taylor columns. *J. Geophys. Res. Oceans*, **120**, 547–562, https://doi.org/10.1002/2014JC010462.

—— , and Coauthors, 2023: Tracing the impacts of recent rapid sea ice changes and the A68 megaberg on the surface freshwater balance of the Weddell and Scotia Seas. *Philos. Trans. Roy. Soc.*, **A381**, 20220162, https://doi.org/10.1098/rsta.2022.0162.

Merino, N., J. Le Sommer, G. Durand, N. C. Jourdain, G. Madec, P. Mathiot, and J. Tournadre, 2016: Antarctic icebergs melt over the Southern Ocean: Climatology and impact on sea ice. *Ocean Modell.*, **104**, 99–110, https://doi.org/10.1016/j.ocemod.2016.05.001.

Morlighem, M., and Coauthors, 2020: Deep glacial troughs and stabilizing ridges unveiled beneath the margins of the Antarctic ice sheet. *Nat. Geosci.*, **13**, 132–137, https://doi.org/10.1038/s41561-019-0510-8.

Mote, T. L., 2007: Greenland surface melt trends 1973–2007: Evidence of a large increase in 2007. *Geophys. Res. Lett.*, **34**, L22507, https://doi.org/10.1029/2007GL031976.

—— , 2014: MEaSUREs Greenland surface melt daily 25km EASE-Grid 2.0, version 1. NASA National Snow and Ice Data Center Distributed Active Archive Center, Accessed 1 December 2024, https://doi.org/10.5067/MEASURES/CRYOSPHERE/nsidc-0533.001.

—— , and M. R. Anderson, 1995: Variations in snowpack melt on the Greenland ice sheet based on passive-microwave measurements. *J. Glaciol.*, **41**, 51–60, https://doi.org/10.3189/S0022143000017755.

Mottram, R., and Coauthors, 2021: What is the surface mass balance of Antarctica? An intercomparison of regional climate model estimates. *Cryosphere*, **15**, 3751–3784, https://doi.org/10.5194/tc-15-3751-2021.

Neuhaus, S. U., and D. R. MacAyeal, 2012: Iceberg drift trajectory follows sea-floor spreading features. 2012 Fall Meeting, San Francisco, CA, Amer. Geophys. Union, Abstract T41B-2596.

Newman, P. A., J. S. Daniel, D. W. Waugh, and E. R. Nash, 2007: A new formulation of equivalent effective stratospheric chlorine (EESC). Atmos. *Chem. Phys.*, **7**, 4537–4552, https://doi.org/10.5194/acp-7-4537-2007.

Norwegian Polar Institute, 2018: Quantarctica v3.0, detailed basemap. Accessed 12 September 2020, https://www.npolar.no/quantarctica/.

Orsi, A. H., T. Whitworth III, and W. D. Nowlin Jr., 1995: On the meridional extent and fronts of the Antarctic Circumpolar Current. *Deep-Sea. Res. I*, **42**, 641–673, https://doi.org/10.1016/0967-0637(95)00021-W.

Oschlies, A., P. Brandt, L. Stramma, and S. Schmidtko, 2018: Drivers and mechanisms of ocean deoxygenation. *Nat. Geosci.*, **11**, 467–473, https://doi.org/10.1038/s41561-018-0152-2.

Otosaka, I. N., and Coauthors, 2023: Mass balance of the Greenland and Antarctic ice sheets from 1992 to 2020. *Earth Syst. Sci. Data*, **15**, 1597–1616, https://doi.org/10.5194/essd-15-1597-2023.

Park, Y.-H., E. Charriaud, and M. Fieux, 1998: Thermohaline structure of the Antarctic surface water/winter water in the Indian sector of the Southern Ocean. *J. Mar. Syst.*, **17**, 5–23, https://doi.org/10.1016/S0924-7963(98)00026-8.

Pezzi, L. P., and Coauthors, 2023: Southern Ocean [in "State of the Climate in 2022"]. *Bull. Amer. Meteor. Soc.*, **104** (9), S351–S355, https://doi.org/10.1175/BAMS-D-23-0077.1.

Purich, A., and E. W. Doddridge, 2023: Record low Antarctic sea ice coverage indicates a new sea ice state. *Commun. Earth Environ.*, **4**, 314, https://doi.org/10.1038/s43247-023-00961-9.

Raphael, M. N., T. J. Maierhofer, R. L. Fogt, W. R. Hobbs, and M. S. Handcock, 2025: A twenty-first century structural change in Antarctica's sea ice system. *Commun. Earth Environ.*, **6**, 131, https://doi.org/10.1038/s43247-025-02107-5.

Reid, P., S. Stammerjohn, R. A. Massom, S. Barreira, T. Scambos, and J. L. Lieser, 2024: Sea ice extent, concentration, and seasonality [in "State of the Climate in 2023"]. *Bull. Amer. Meteor. Soc.*, **105** (8), S351–S354, https://doi.org/10.1175/BAMS-D-24-0099.1.

——, and R. A. Massom, 2022: Change and variability in Antarctic coastal exposure, 1979–2020. *Nat. Commun.*, **13**, 1164, https://doi.org/10.1038/s41467-022-28676-z.

Reynolds, R. W., N. A. Rayner, T. M. Smith, D. C. Stokes, and W. Wang, 2002: An improved in situ and satellite SST analysis for climate. *J. Climate*, **15**, 1609–1625, https://doi.org/10.1175/1520-0442(2002)015<1609:AIISAS>2.0.CO;2.

Riihelä, A., R. M. Bright, and K. Anttila, 2021: Recent strengthening of snow and ice albedo feedback driven by Antarctic sea-ice loss. *Nat. Geosci.*, **14**, 832–836, https://doi.org/10.1038/s41561-021-00841-x.

Roemmich, D., and J. Gilson, 2009: The 2004–2008 mean and annual cycle of temperature, salinity, and steric height in the global ocean from the Argo Program. *Prog. Oceanogr.*, **82**, 81–100, https://doi.org/10.1016/j.pocean.2009.03.004.

Sabu, P., S. A. Libera, R. Chacko, N. Anilkumar, M. P. Subeesh, and A. P. Thomas, 2020: Winter water variability in the Indian Ocean sector of Southern Ocean during austral summer. *Deep-Sea Res. II*, **178**, 104852, https://doi.org/10.1016/j.dsr2.2020.104852.

Santee, M. L., and Coauthors, 2024: The influence of stratospheric hydration from the Hunga eruption on chemical processing in the 2023 Antarctic vortex. *J. Geophys. Res. Atmos.*, **129**, e2023JD040687, https://doi.org/10.1029/2023JD040687.

Sathyendranath, S., and Coauthors, 2019: An ocean-colour time series for use in climate studies: The experience of the Ocean-Colour Climate Change Initiative (OC-CCI). *Sensors*, **19**, 4285, https://doi.org/10.3390/s19194285.

Scambos, T., R. Ross, R. Bauer, Y. Yermolin, P. Skvarca, D. Long, J. Bohlander, and T. Haran, 2008: Calving and ice-shelf breakup processes investigated by proxy: Antarctic tabular iceberg evolution during northward drift. *J. Glaciol.*, **54**, 579–591, https://doi.org/10.3189/002214308786570836.

——, E. Berthier, T. Haran, C. A. Shuman, A. J. Cook, S. R. M. Ligtenberg, and J. Bohlander, 2014: Detailed ice loss pattern in the northern Antarctic Peninsula: Widespread decline driven by ice front retreats. *Cryosphere*, **8**, 2135–2145, https://doi.org/10.5194/tc-8-2135-2014.

——, and Coauthors, 2024: Life cycle of icebergs B-15 and C-19. 2024 Fall Meeting, Washington, D.C., Amer. Geophys. Union, Abstract C21F-0423.

Smith, B., and Coauthors, 2020: Pervasive ice sheet mass loss reflects competing ocean and atmosphere processes. *Science*, **368**, 1239–1242, https://doi.org/10.1126/science.aaz5845.

——, S. Dickinson, B. P. Jelley, T. A. Neumann, D. Hancock, J. Lee, and K. Harbeck, 2022: ATLAS/ICESat-2 L3B slope-corrected land ice height time series, version 5. NASA National Snow and Ice Data Center Distributed Active Archive Center, accessed 18 February 2024, https://doi.org/10.5067/ATLAS/ATL11.005.

Spira, T., S. Swart, I. Giddy, and M. Du Plessis, 2024: The observed spatiotemporal variability of Antarctic Winter Water. *J. Geophys. Res. Oceans*, **129**, e2024JC021017, https://doi.org/10.1029/2024JC021017.

Stammerjohn, S. E., D. G. Martinson, R. C. Smith, X. Yuan, and D. Rind, 2008: Trends in Antarctic annual sea ice retreat and advance and their relation to El Niño–Southern Oscillation and Southern Annular Mode variability. *J. Geophys. Res.*, **113**, C03S90, https://doi.org/10.1029/2007JC004269.

Stern, A. A., A. Adcroft, and O. Sergienko, 2019: Modeling ice shelf cavities and tabular icebergs using Lagrangian elements. *J. Geophys. Res. Oceans*, **124**, 3378–3392, https://doi.org/10.1029/2018JC014876.

Swithinbank, C., K. Brunk, and J. Sievers, 1988: A glaciological map of Filchner-Ronne ice shelf, Antarctica. *Ann. Glaciol.*, **11**, 150–155, https://doi.org/10.3189/S0260305500006467.

Taylor, G. I., 1922: The motion of a sphere in a rotating liquid. *Proc. Roy. Soc. London*, **102A**, 180–189, https://doi.org/10.1098/rspa.1922.0079.

The Firn Symposium Team, 2024: Firn on ice sheets. *Nat. Rev. Earth Environ.*, **5**, 79–99, https://doi.org/10.1038/s43017-023-00507-9.

The IMBIE Team, 2019: Mass balance of the Greenland Ice Sheet from 1992 to 2018. *Nature*, **579**, 233–239, https://doi.org/10.1038/s41586-019-1855-2.

Thomalla, S., S. Nicholson, T. J. Ryan-Keogh, and M. Smith, 2023: Widespread changes in Southern Ocean phytoplankton blooms linked to climate drivers. *Nat. Climate Change*, **13**, 975–984, https://doi.org/10.1038/s41558-023-01768-4.

——, and Coauthors, 2024: Southern Ocean [in "State of the Climate in 2023"]. *Bull. Amer. Meteor. Soc.*, **105** (8), S355–S356, https://doi.org/10.1175/BAMS-D-24-0099.1.

Thomas, D. N., Ed., 2017: *Sea Ice.* 3rd ed. Wiley-Blackwell, 664 pp.

Trusel, L. D., J. D. Kromer, and R. T. Datta, 2023: Atmospheric response to Antarctic sea-ice reductions drives ice sheet surface mass balance increases. *J. Climate*, **36**, 6879–6896, https://doi.org/10.1175/JCLI-D-23-0056.1.

Turner, J., and Coauthors, 2004: The SCAR READER project: Toward a high-quality database of mean Antarctic meteorological observations. *J. Climate*, **17**, 2890–2898, https://doi.org/10.1175/1520-0442(2004)017<2890:TSRPTA>2.0.CO;2.

—— , and Coauthors, 2019: The dominant role of extreme precipitation events in Antarctic snowfall variability. *Geophys. Res. Lett.*, **46**, 3502–3511, https://doi.org/10.1029/2018GL081517.

van Wessem, J. M., and Coauthors, 2018: Modelling the climate and surface mass balance of polar ice sheets using RACMO2 – Part 2: Antarctica (1979–2016). *Cryosphere*, **12**, 1479–1498, https://doi.org/10.5194/tc-12-1479-2018.

Wang, H., J. G. Fyke, J. T. M. Lenaerts, J. M. Nusbaumer, H. Singh, D. Noone, P. J. Rasch, and R. Zhang, 2020: Influence of sea-ice anomalies on Antarctic precipitation using source attribution in the Community Earth System Model. *Cryosphere*, **14**, 429–444, https://doi.org/10.5194/tc-14-429-2020.

Wang, Y., D. Zhou, A. Bunde, and S. Havlin, 2016: Testing reanalysis data sets in Antarctica: Trends, persistence properties, and trend significance. *J. Geophys. Res. Atmos.*, **121**, 12 839–12 855, https://doi.org/10.1002/2016JD024864.

Wiese, D. N., D.-N. Yuan, C. Boening, F. W. Landerer, and M. M. Watkins, 2023a: JPL GRACE Mascon ocean, ice, and hydrology equivalent water height RL06.1 CRI filtered version 03. Ver. RL06.1Mv03. PO.DAAC, accessed 10 February 2023, https://doi.org/10.5067/TEMSC-3JC63.

—— , —— , —— , —— , and —— , 2023b: Tellus level-4 ocean mass anomaly time series from JPL GRACE/GRACE-FO Mascon CRI filtered release 06.1 version 03. Ver. RL06.1Mv03. PO.DAAC, accessed 10 February 2023, https://doi.org/10.5067/TEMSC-AT613.

Wille, J. D., and Coauthors, 2021: Antarctic atmospheric river climatology and precipitation impacts. *J. Geophys. Res. Atmos.*, **126**, e2020JD033788, https://doi.org/10.1029/2020JD033788.

Wong, A. P. S., and Coauthors, 2020: Argo data 1999–2019: Two million temperature-salinity profiles and subsurface velocity observations from a global array of profiling floats. *Front. Mar. Sci.*, **7**, 700, https://doi.org/10.3389/fmars.2020.00700.